The Bunburra Rockhole meteorite fall in SW Australia: fireball trajectory, luminosity, dynamics, orbit, and impact position from photographic and photoelectric records

Pavel SPURNÝ^{1*}, Philip A. BLAND^{2,3,4}, Lukáš SHRBENÝ¹, Jiří BOROVIČKA¹, Zdeněk CEPLECHA¹, Andrew SINGELTON⁵, Alex W. R. BEVAN⁶, David VAUGHAN⁷, Martin C. TOWNER², Terence P. McCLAFFERTY⁸, Ralf TOUMI⁵, and Geoff DEACON³

¹Astronomical Institute, Academy of Sciences CR, Fričova 298, 25165 Ondřejov Observatory, Czech Republic ²Impacts & Astromaterials Research Centre (IARC), Department of Earth Science & Engineering, Imperial College London, London SW7 2AZ, UK

³IARC, Department of Mineralogy, Natural History Museum, London SW7 5BD, UK
 ⁴Department of Applied Geology, Curtin University, G.P.O. Box U1987, Perth, Western Australia 6845, Australia
 ⁵Blackett Laboratory, Department of Physics, Imperial College London, London SW7 2AZ, UK
 ⁶Department of Earth and Planetary Sciences, Western Australian Museum, Locked Bag 49, Welshpool DC, Western Australia 6986, Australia

⁷P.O. Box 187, Subiaco, Perth, Western Australia 6000, Australia ⁸Office of Research and Development, Curtin University, G.P.O. Box U1987, Perth, Western Australia 6845, Australia *Corresponding author. E-mail: spurny@asu.cas.cz

(Received 21 July 2011; revision accepted 23 November 2011)

Abstract-We report an analysis of the first instrumentally observed meteorite fall in Australia, which was recorded photographically and photoelectrically by two eastern stations of the Desert Fireball Network (DFN) on July 20, 2007. The meteoroid with an initial mass of 22 kg entered the atmosphere with a low speed of 13.36 km s⁻¹ and began a luminous trajectory at an altitude of 62.83 km. In maximum, it reached -9.6 absolute magnitude and terminated after a 5.7 s and 64.7 km long flight at an altitude of 29.59 km with a speed of 5.8 km s⁻¹. The angle of the atmospheric trajectory to the Earth's surface was 30.9°. The first organized search took place in October 2008 and the first meteorite (150 g) was found 97 m southward from the predicted central line at the end of the first day of searching (October 3, 2008). The second stone (174 g) was recovered 39 m northward from the central line, both exactly in the predicted mass limits. During the second expedition in February 2009, a third fragment of 14.9 g was found again very close (~100 m) from the predicted position. Total recovered mass is 339 g. The meteorite was designated Bunburra Rockhole (BR) after a nearby landscape structure. This first DFN sample is an igneous achondrite. Initial petrography indicated that BR was a brecciated eucrite but detailed analyses proved that BR is not a typical eucrite, but an anomalous basaltic meteorite (Bland et al. 2009). BR was delivered from an unusual, Aten type orbit (a < 1 AU) where virtually the entire orbit was contained within Earth's orbit. BR is the first achondrite fall with a known orbit and it is one of the most precise orbits ever calculated for a meteorite dropping fireball.

INTRODUCTION

Instrumental observations of fireballs, especially those that can produce meteorites, are of great scientific interest and importance because meteorites provide us with a surviving physical record of the formation of our solar system, and a direct link to their parent asteroids. But meteorites are also unique—as geological materials—in that they come with virtually no spatial context to aid us in interpreting that record. There is a profound disconnect with possible parent bodies, asteroids and comets, in our data. We have no similar sample-return material yet, and

reliable orbital information for meteorite falls is known for only a dozen cases, in contrast with tens of thousands meteorites already collected and classified. So every new case with precise orbital data gives us invaluable information about the complex mosaic that makes up the population and physical characteristic of small interplanetary bodies in near-Earth space and also about their parents—asteroids and comets.

Similarly important is the study of processes accompanying the atmospheric flight of the meteoroid producing a meteorite fall. From every new instrumentally documented fall, we learn very much in the sense of refining our methods and models; a process which is also well documented in increased efficiency of successful recoveries over the last few years (Brown et al. 2011). On the other hand, the known properties of the meteorite, such as density, mass, shape, composition, structure, etc., enable reverse calibration of the fireball data so that other fireballs without recovered meteorites, whether they were too small for the fall or never recovered, can provide relevant information on the physical properties of their respective meteoroids.

There is a paucity of possible methods for linking specific meteorites or meteorite classes with their parent asteroids. Partially it can be examined by direct spacecraft encounters with asteroids (e.g., Ida, Gaspra, and Eros; Chapman 2004), or via asteroid sample-return missions (currently only the Hayabusa mission; Yano et al. 2006). These are necessarily limited to only a few parent bodies. In light of the scarcity and also high costs of such in situ missions, determining meteoroid preimpact orbits from instrumental observations of atmospheric flight, and subsequent meteorite recoveries, remains an efficient way to resolve linkages between recovered meteorites and their parents. The best way to observe fireballs and determine their preimpact orbits, and also triangulate fall positions and recover meteorites, is camera networks. Here, we present analysis of the first meteorite fall that was recorded photographically and photoelectrically by two automated fireball observatories of the Desert Fireball Network (DFN). As it was only a meteoroid—approximately the size football-which flew over very remote and uninhabited areas of the Nullarbor Plain of SW Australia, there was no other observation or detection than from our dedicated project. Altogether three meteorites with a total mass of 339 g were recovered in the predicted area. This is the first DFN meteorite and also the first instrumentally detected meteorite fall from the southern hemisphere.

This article is devoted to the detailed analysis of all available fireball data, i.e., to determination of the fireball atmospheric trajectory, dynamics, luminosity, heliocentric orbit, and impact position from photographic



Fig. 1. Autonomous fireball observatory at the station DFO 02.

and photoelectric records. We also describe the circumstances of data acquisition and meteorite recoveries.

DATA ACQUISITION

Instruments

The reported fireball and meteorite fall was captured by the DFN, an ambitious project dedicated to the mapping of fireballs over the Nullarbor Region of southwestern Australia, a very suitable place for meteorite recoveries (Bland 2004).

For an observing system, we wanted to use an already well-tested imaging system that proved to be suitable for precise positional and dynamic information. To satisfy all these basic requirements, we have modified the autonomous fireball observatory (AFO) already developed by Spurný and co-workers for the European Network (Spurný and Borovička 2002; Spurný et al. 2006). Although this unit was designed to work in very different conditions (i.e., the temperate zone in Europe), we were able to modify it to operate in severe desert conditions: exposure to a very wide range of temperatures (some nights temperature can drop well below the freezing point, and on the other hand it can be over 50 °C during summer days), electrical and dust storms, and the red dust that is ever-present in Australian deserts, etc. The result is a desert fireball observatory (DFO) (see Fig. 1). In December 2005, we established a small network consisting of three stations in the Nullarbor Region of southwestern Australia. The fourth station was set up in November 2007 (see Fig. 2). Each station is equipped with the DFO, solar power station, and satellite data link (see Fig. 3). Thus far, our preliminary network of four DFOs has allowed us to accumulate a data set of complete and precise

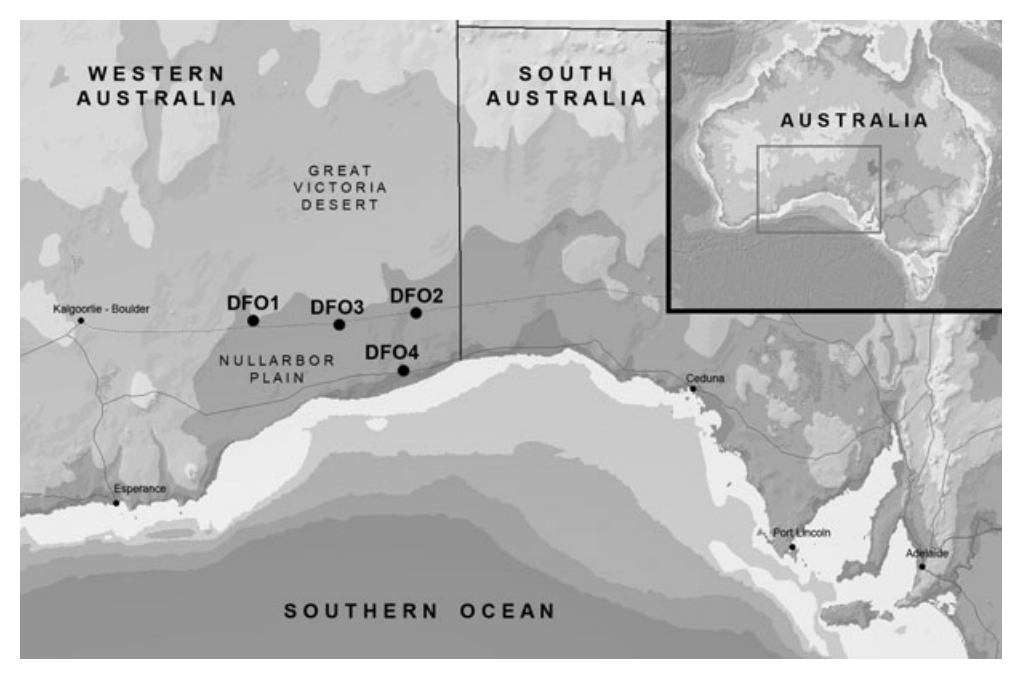


Fig. 2. Schematic map showing the arrangement of the stations of the Australian Desert Fireball Network.

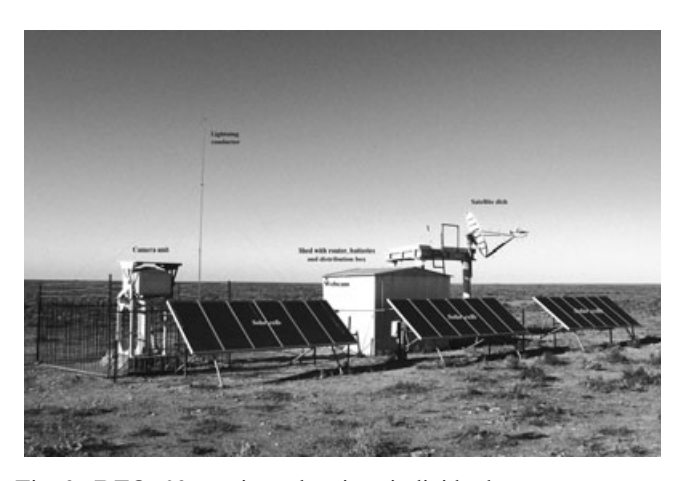


Fig. 3. DFO 03 station showing individual components as displayed at each of the Desert Fireball Network stations.

atmospheric trajectories, orbits, light curves, and dynamics for around 200 fireballs. Among others, these are the first orbital data for southern hemisphere fireballs. Here, we report on one of the most important achievement of the DFN so far: the Bunburra Rockhole meteorite fall.

Photographic Data

The fireball designated DN200707B (DN means Desert Network and number is the date in the format DDMMYY; B indicates the second fireball on that particular night), and lately named Bunburra Rockhole

(see the Searching for Meteorites and Their Recovery section), was recorded by two eastern stations DFO 02 and DFO 03 of the DFN on July 20, 2007. The station DFO 04, which would be the closest station to the fireball trajectory, was set up about 4 months later and the station DFO 01 was too far to record this moderately bright fireball. Both stations had a perfectly clear sky, not only at the time of the fireball passage, but for almost all of this night, including the beginning and end of the exposure. This was important for two main reasons. First, the transparent sky enables us to measure more details on the fireball luminous path including breaks (time marks on the luminous path enabling velocity determination), and perfect sky conditions also significantly helped in the correct reduction of both images because we had enough reference stars to precisely define the coordinate system on each image and determine the coordinates of each measured point on the fireball luminous trajectory. This was a very important factor because the geometry was far from ideal and the fireball was quite close to the horizon on both stations, especially on DFO 03 where angular heights above the horizon varied in the range from only 9.7° to 5.8°. The situation on the DFO 02 image was better but the fireball was still only 18.7° above the ideal horizon for the beginning, and 12.9° for the end. This case completely proved our methodology in using large format fish-eye lenses (Zeiss Distagon 3.5/30 mm) in combination with photographic film (Ilford FP4 sheet film 9×12 cm, one per night). Thanks to the precise

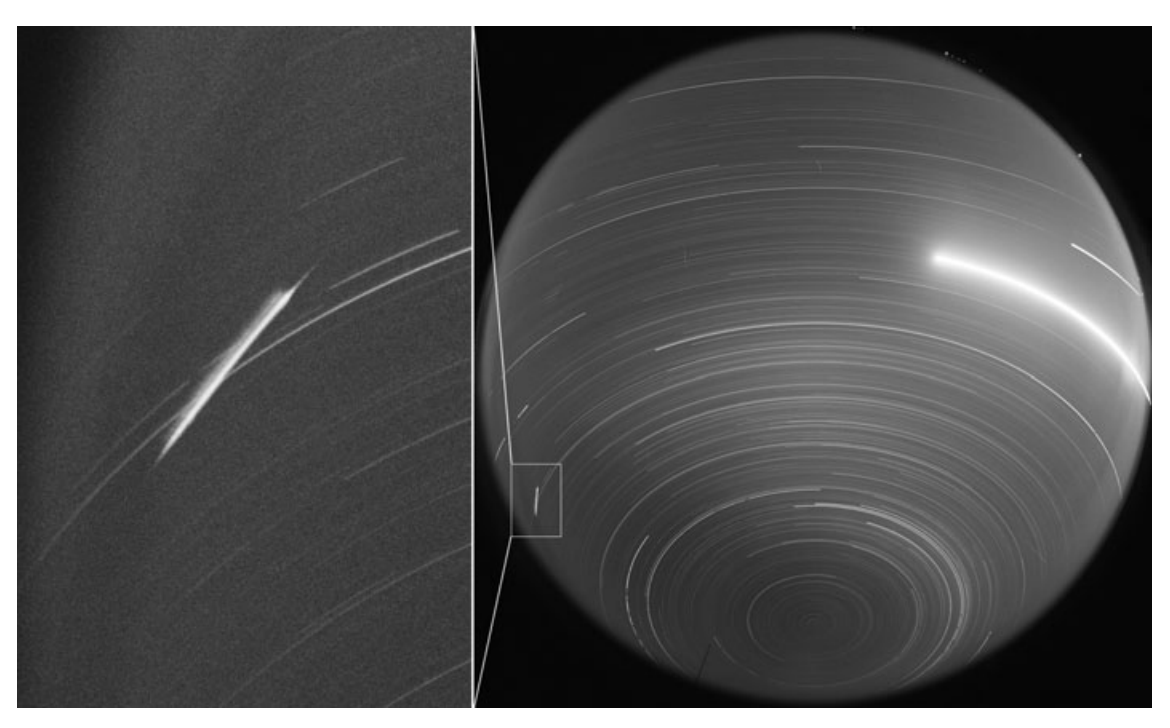


Fig. 4. All-sky image and detail containing the Bunburra Rockhole fireball as recorded by the DFO 02 station. The fireball is close to the ESE horizon and 188–127 km far from the station. This all-night long exposure took 11^h40^m. The brightest trail on the west belongs to Moon near the first quarter.

imaging and high resolution of both images (we scan and measure each point with precision of 5 µm) we were able not only to reduce both images but, as we outline below, also to determine the atmospheric trajectory and dynamics with surprisingly high precision. An all-sky image with detail of the fireball from the closest station DFO 02 is shown in Fig. 4, and from station DFO 03 in Fig. 5. The image from DFO 03 station was used only for trajectory determination because, due to bad geometry (the fireball flew almost directly over the station), breaks were too close to each other to be measurable. It is interesting to mention that for the complete description of this meteorite fall we had the minimum of necessary records, i.e., only two images to determine trajectory and only one image with velocity data. Of course, this makes the entire task significantly more difficult as there is no independent check of individual results (trajectory position, velocity). However, as will be shown later, the main proof that all presented data are correct is the recovery of meteorites at the predicted locations and with predicted masses.

Photoelectric Data

Along with direct photographic recording each DFO (and AFO as well) contains a fast linear photometer which records the total illumination of the sky with a

rate of 500 samples per second. The sensitivity of these photometers corresponds almost exactly to the photographic sensitivity of the imaging system. The original intention for the implementation of these instruments into automated observatories was to have an exact time for each photographed fireball. This is also the reason why the internal time of this photometer is continuously corrected. At the time of the Bunburra Rockhole fall, this was achieved via a data link and time servers and we recorded the time with a precision of approximately 0.01 s. Currently we use the PPS signal from the GPS satellite system, which provides significantly improved precision (better than 0.1 ms). From both photometers, we got independently the same absolute time for the event at $19^{h}13^{m}57.32^{s} \pm 0.01^{s}$ UT. This time is valid for the very sharp apparent maximum flare near the end of the luminous trajectory. However, these photometers have much wider utility. In addition to providing the exact time of the event, we have a very detailed light curve for each event which is bright enough to have a good s/n ratio. Fortunately, it was the case of the BR fireball (at least for the closer station—DFO 02). This is well documented in Fig. 6, where an apparent light curve from the DFO 02 station is shown. All features visible on this light curve are real because the noise is very low, as can be seen near the beginning and end where no signal from the fireball is present. Figure 7

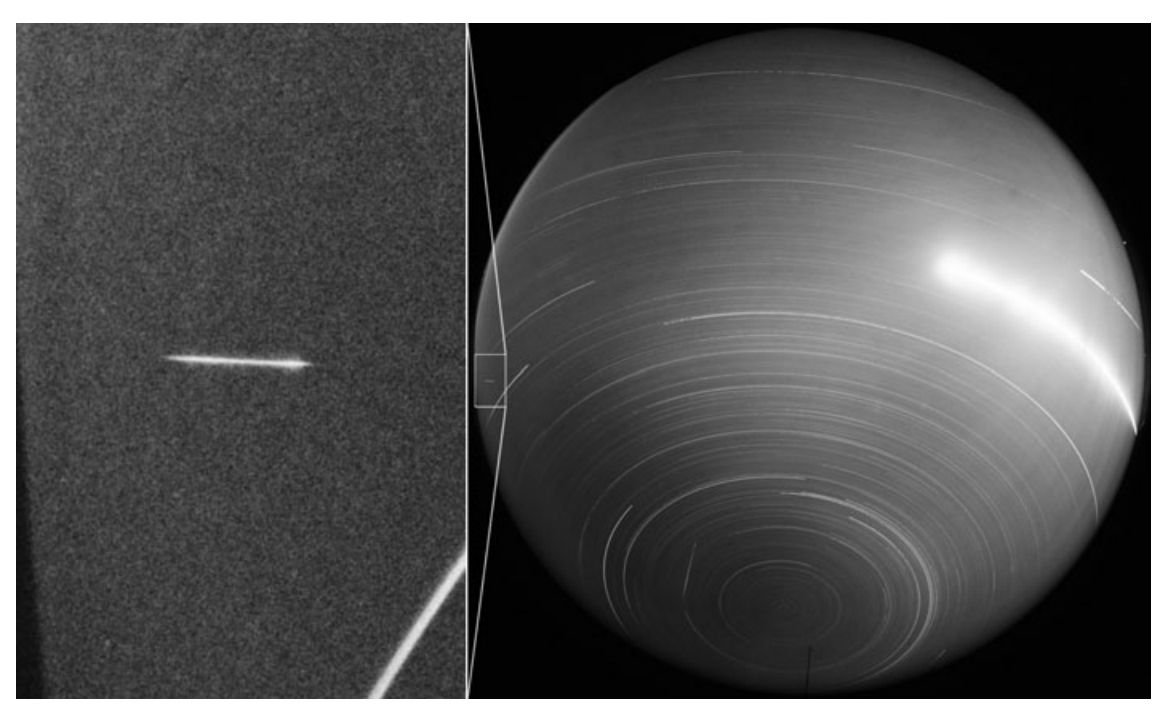


Fig. 5. All-sky image and detail containing the Bunburra Rockhole fireball as recorded by the DFO 03 station. The fireball is close to the eastern horizon and 316–264 km far from the station. This all-night long exposure took 11^h35^m and partly was affected by high altitude clouds. Another fireball (DN200707A) can be seen on the SW close to the South Pole. This fireball (seen also on the DFO 02 image) completely disintegrated at a height of 39.7 km.

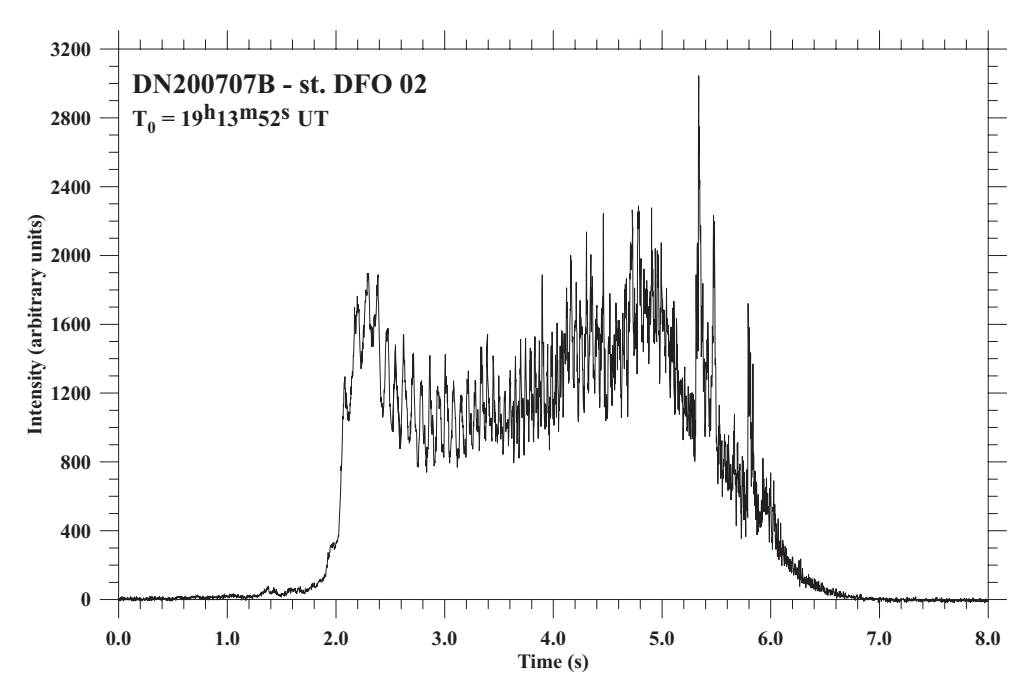


Fig. 6. Apparent (not corrected) light curve taken by the photoelectric photometer of the DFO 02 with time resolution of 500 samples per second. Noise is almost negligible in the scale of the plot.

shows the same light curve from the DFO 03 photometer. It is noteworthy that both light curve profiles, with high fidelity, are very similar. Only the

DFO 03 record has a much smaller s/n ratio as the fireball was much farther away, and also closer to horizon than on the DFO 02 station (see also Figs. 4 and

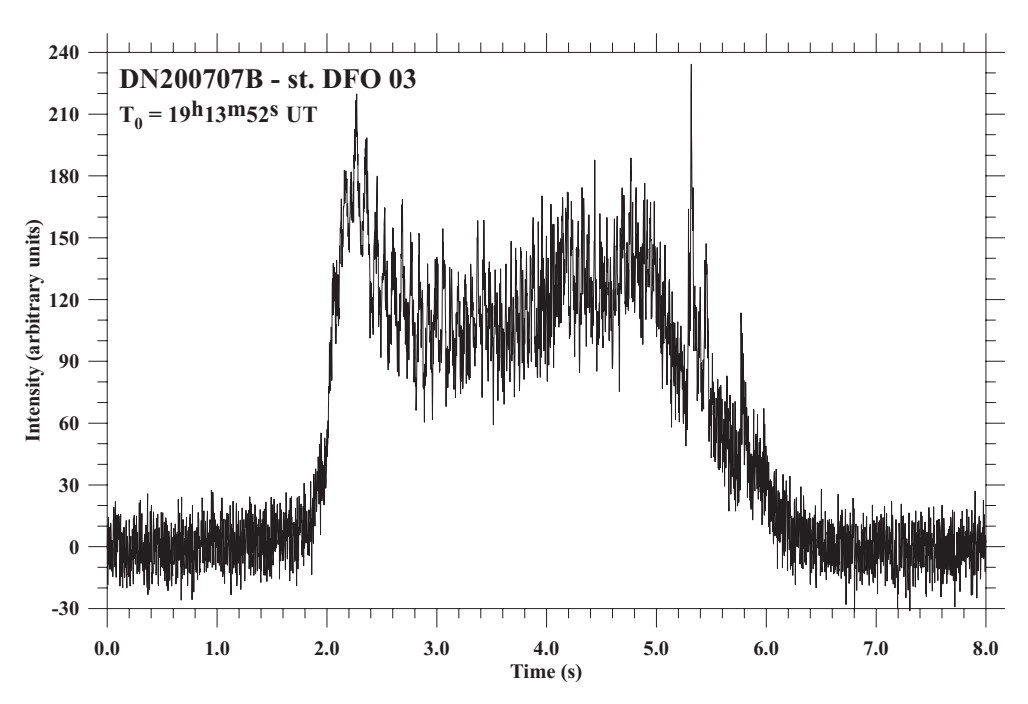


Fig. 7. Apparent (not corrected) light curve taken by the photoelectric photometer of the DFO 03 station with time resolution of 500 samples per second. Much higher noise is caused by much lower signal due to the significantly larger distance of the station from the fireball.

5). Many details, especially on the light curve from DFO 02, are visible including fast fluctuations of light at the beginning and middle parts of the fireball. These light curves will be discussed later in the Photographic and Photoelectric Photometry section.

Photometers in DFOs/AFOs have an important function. The photoelectric record is analyzed in each camera in real time to identify fireballs. This automated check is very reliable and useful especially for brighter events. If the camera diagnoses some event which resembles a fireball, and if this record is above a given threshold (combination of average s/n ratio with duration of the event), the camera sends a warning e-mail with such details as beginning and end time of the event, its duration and peak, and average signal value. This was the case for the BR fireball from DF0 02, so that we had immediate information that we had recorded an interesting fireball. All such events are stored in each DFO separately so it is simple to download the individual light curves and see immediately the importance of each particular event. In the case of the BR fireball, we saw on the downloaded light curves important indices (duration of the event, gradual decrease of light near the end, type of the light curve which corresponded to the type I fireballs) that it could be a meteorite fall. It was confirmed about 2 months later when we received the images from both cameras and did the first trajectory computations.

Table 1. Atmospheric trajectory data on the Bunburra Rockhole fireball.

	Beginning	Terminal
Velocity (km s ⁻¹)	13.31 ± 0.02	5.68 ± 0.12
Height (km)	62.83 ± 0.03	29.59 ± 0.02
Longitude (°E)	$129.82721 \ \pm \ 0.00018$	129.25555 ± 0.00015
Latitude (°S)	-31.4496 ± 0.0003	-31.3710 ± 0.0002
Mass (kg)	22.	1.1
Slope (°)	31.19 ± 0.03	30.70 ± 0.03
Total length (km)/		
duration (s)	64.65/5.68	
Maximum	-9.6 ± 0.1	
absolute		
magnitude		
Fireball type/PE	I/-4.47	
DN stations No.	DFO 02, DFO 03	

ATMOSPHERIC TRAJECTORY

The reported fireball occurred over SW Australia on July 20, 2007 at $19^h 13^m 53.24^s \pm 0.05^s$ UT. This time is valid for the photographic beginning, i.e., it corresponds to the first measured point in Table 1 where all basic atmospheric trajectory values are listed. This is the reason why the standard deviation is approximately $5\times$ higher than the internal precision of time for each photometer, as is discussed in a previous section. In local time, the event occurred on July 21 at $3^h 13^m 53^s$ WST,

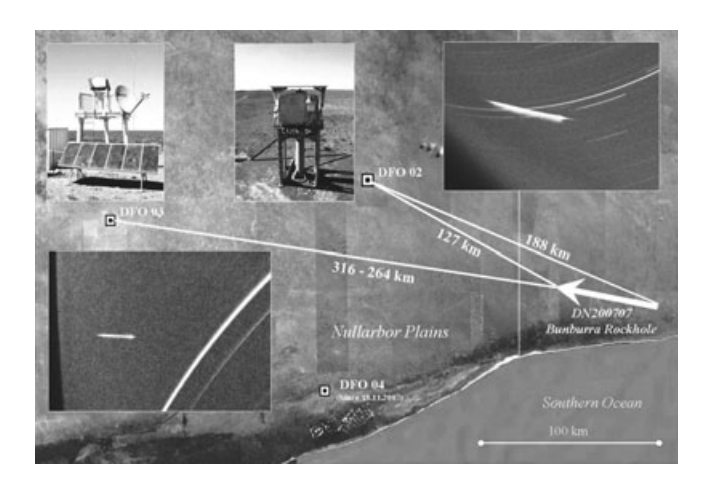


Fig. 8. Schematic map of the Nullarbor area containing Desert Fireball Network stations with the images of automated desert fireball observatories, details of all-sky records of the DN200707 Bunburra Rockhole fireball, and projection of its luminous trajectory on the ground.

about 2 h and 10 min before the end of the planned exposure, so in reality it was a morning fall.

After measurements of scanned high resolution copies of the original images, we reduced both all-sky records and computed the atmospheric trajectory of the recorded fireball. We found that the geometry was unfortunately not very good because the entire trajectory was far on the southeast out of the network area and the fireball flew practically toward the station DFO 03, so its apparent path on the image was very short (see Fig. 5). On the other hand, the intersection angle between planes from the stations was 52° which increased the reliability of the given solution. As was mentioned in the Photographic Data section, the fireball was very close to the horizon at both stations. The distance from the first, closer station DFO 02, varied from 188 km in the beginning to 127 km at the end point; and for the second station DFO 03 it varied from 316 to 264 km. This situation is schematically displayed in Fig. 8. One very important aspect from the atmospheric trajectory solution was that the fireball flew and especially terminated over land, which was obviously crucial for the possible search for meteorites.

The fireball's luminous trajectory started—i.e., it reached the sensitivity limit of the photographic system which was in this case about -2.5 magnitude (apparent value)—at an altitude of 62.83 km, and after a 64.7 km long flight it terminated at an altitude of 29.59 km. The angle of the atmospheric trajectory to the Earth's surface was 30.9°. The object, with initial mass of about 22 kg and size of a football, entered the atmosphere with a very low speed of 13.36 km s⁻¹, and during a 5.7 s long flight decelerated to the terminal speed of 5.8 km s⁻¹, when the fireball brightness decreased below sensitivity limit of

both DFOs. Fireball speed is determined from time marks (breaks), which are produced by a three-blade revolving sector with rotation speed 7 Hz located close above the film emulsion and resulting in 21 breaks per second.

PHOTOGRAPHIC AND PHOTOELECTRIC PHOTOMETRY

For the determination of the fireball photometry, we used both available observing methods which our observing system provides us—the standard photometry on the photographic image and the photoelectric (radiometric) photometry on the calibrated brightness sensor record, both from the DFO 02 camera. The DFO 03 radiometric record served only as an independent check of the light curve fidelity and absolute timing of the fireball passage.

The absolute brightness (corrected on the 100 km distance) was determined from the standard photometry (i.e., film density) of the DFO 02 photographic image using our own software FishScan (created by J. Borovička, described in Spurný et al. 2006). This software serves for positional and photometric measuring of fireballs on the high resolution scanned copies of the original films using the photogrammetric scanner Vexcel Ultrascan 5000 to save the metric precision of the original film and sufficient photometric information (14 bits density) as well.

FishScan photometry is the method that uses the darkening of star trails on scanned negatives to determine the characteristic density curve and meteor brightness. Before the measurement, the image is corrected for decreasing sensitivity with the distance from the center of projection (i.e., flat-fielded) using the factory curve for the Zeiss Distagon lens that is used in the DFOs. The measured darkening of a star trail is corrected for star trailing velocity caused by daily motion. Stars are measured over a wide interval of zenith distances, and the actual extinction coefficient is determined together with the characteristic curve. When converting meteor darkening into magnitudes, the difference due to occultation by the rotating shutter (star images are occulted by the shutter in contrast to the fireball image) and the fireball trailing velocity are taken into account. Properties of photographic film are at very low light levels and exposures of longer than about 1 s described by Schwarzschild's law that compares degree of blackening. The law says: sources of light of different intensities, I, cause the same degree of blackening under different exposures, t, if the products I^*t^p are equal, where p is the Schwarzschild's coefficient $(p = 0.80 \pm 0.05 \text{ is assumed here})$. As the fireball is often the brightest object on the whole picture and the derived dependencies must be extrapolated, the standard

deviations of fireball brightness may exceed one stellar magnitude in some cases (Shrbený 2009; Shrbený and Spurný 2009). Fortunately, this was not the case for the Bunburra Rockhole fireball, because the fireball was of only moderate brightness and we could use bright planets (Jupiter and Venus) for determination of the characteristic curve. Therefore, the resulting maximum standard deviation is only about 0.2 magnitudes.

Following the procedure described above, absolute brightness of the Bunburra Rockhole fireball was obtained for all 115 measured points (breaks). The maximum absolute (100 km distance) brightness of -9.2 magnitude was reached after a very steep increase, surprisingly near the beginning, at an altitude of 55.7 km. After a small decrease it stayed almost constant for 3 s and near the end, just before the final decrease, the brightness increased again and—in not well distinct flares—reached close to the first maximum (within errors of the measurement). Therefore, it is difficult to say just from the photographic photometry where exactly the maximum of the fireball brightness was. Fortunately, we have an independent light curve from radiometers where we see a complete light profile with much higher time resolution than from photographs where some short events (millisecond flares) can be hidden behind a shutter blade. The rotating shutter, which contains three blades, interrupts a fireball image 21 times in a second, which results in time resolution of a photographic light curve of 0.0475 s. It enables us to determine reliably a basic profile of the light curve and individual brightness of each measured point. However, it is not detailed enough to see and study shapes and details of individual flares and fast changes of brightness such as we discovered on photoelectric light curves for other fireballs observed in the Czech Fireball Network (Spurný and Ceplecha 2008) and which are also presented on the BR light curve as shown in Figs. 6 and 7. We see numerous periodic fast changes in luminosity (in the first half) and very short flares of millisecond duration as well (especially in the second half). And it was exactly the reason why the brightest flare visible near the end on the BR radiometric light curve with duration of only 0.03 s was just eclipsed by the shutter blade on the photograph. As will be shown later, it means that in reality the maximum brightness was reached in this flare at a height of 36.3 km. The resulting maximum absolute magnitude was thus -9.6.

Before we discuss and study these interesting features on the DFO 02 radiometric light curve, it was necessary to make some corrections of the original record (Fig. 6) to arrive at absolute values of intensity. First, the light curve was corrected for decreasing sensitivity of the detector with distance from local zenith. For this purpose, we applied the factory curve for the photomultiplier tube

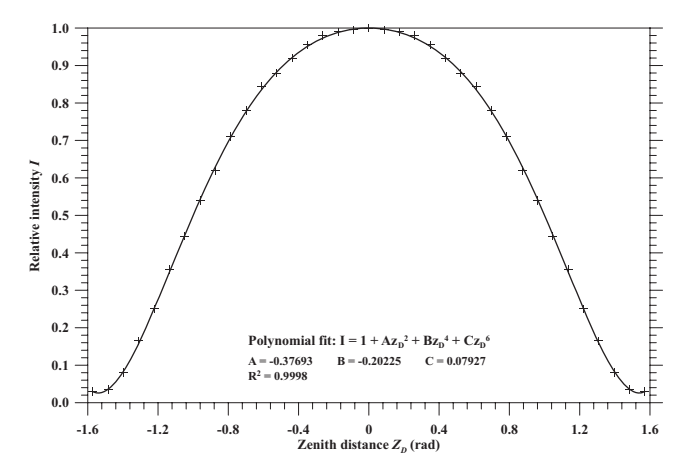


Fig. 9. Dependence of measured values of sensitivity of the DFO photometer on zenith distance and its fit by polynomial of the sixth order which was used for correction.

used in the brightness detector, fitted by a polynomial of sixth order as can be seen in Fig. 9. The next step was correction for changing distance of the fireball from the detector. The observed intensity was recalculated into the absolute unit distance of 100 km. The last step was to obtain the absolute values of brightness, so the photoelectric light curve had to be shifted for an unknown value to fit the photographic one. This shift was determined by fitting the averaged photoelectric light curve on the photographic one by the least square method. The photoelectric light curve was averaged in temporal intervals of 0.0475 s corresponding to the breaks on the fireball image caused by a rotating shutter. The resulting shift is -6.04 magnitudes and the standard deviation between the two curves is 0.24 magnitudes. If we determine the standard deviation only for points being above the noise level of the radiometric light curve, which corresponds to absolute brightness of -6 magnitude, the value of standard deviation is only 0.15 magnitudes, which is comparable with the accuracy of the photographic light curve or even better. The corrected radiometric and photographic light curves of the BR fireball are shown in Fig. 10. The agreement between both light curves is exceedingly good. It demonstrates that these two instrumentally different and independent methods give the same results and that the presented photometric data are very reliable. It also proves that the brightness sensor with all corrections described above can be used as a very precise photometer.

After correction of the photoelectric light curve on absolute values, we can study some interesting features as mentioned above. The noise on this record (from DFO 02 photometer) is very low so all features visible on the light curve are real. It is also supported by the independent record from the DFO 03 brightness sensor

Bunburra Rockhole

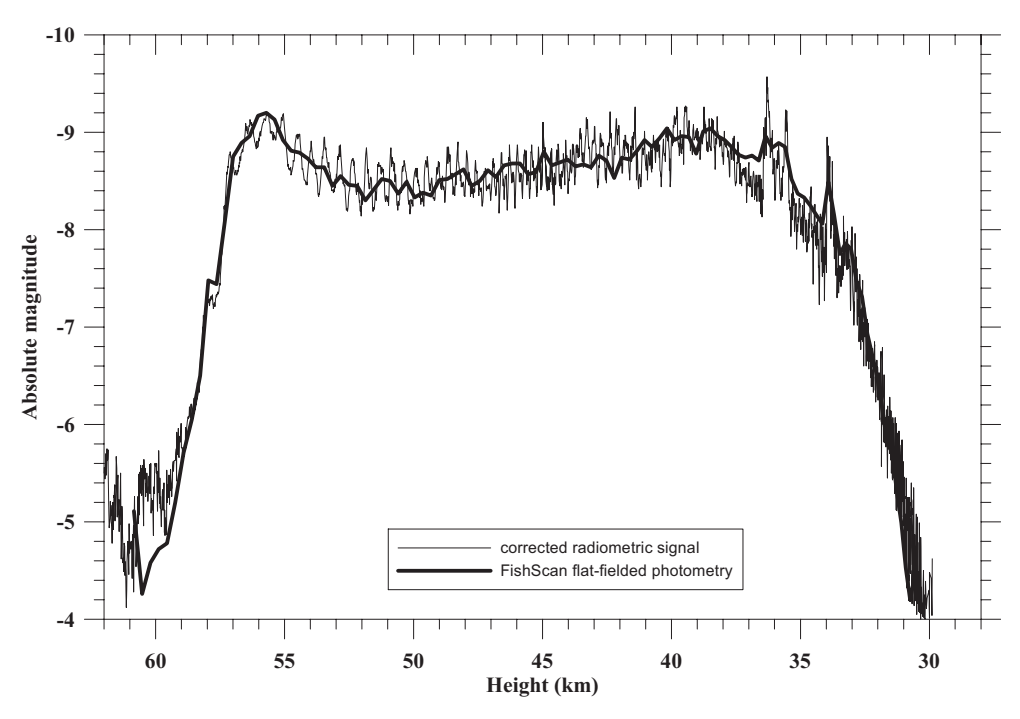


Fig. 10. The corrected radiometric and photographic light curves of the Bunburra Rockhole fireball.

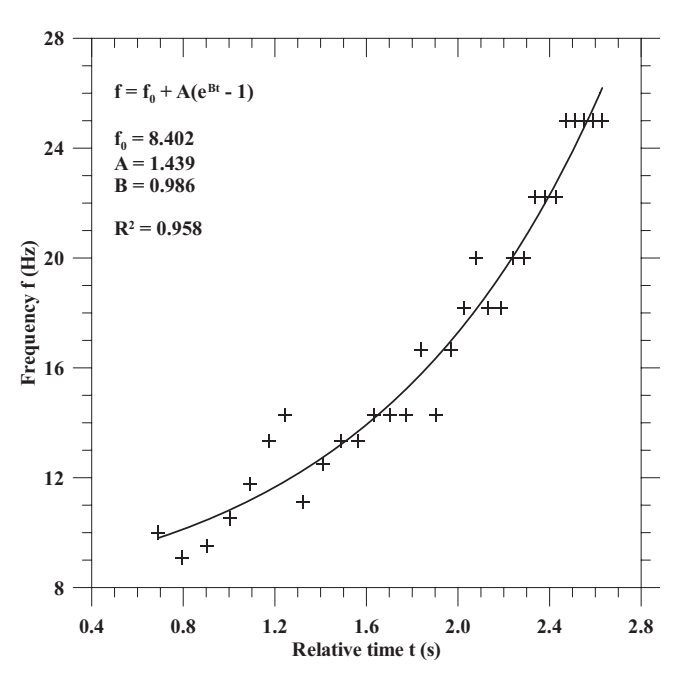


Fig. 11. Frequency of periodic luminosity changes from the DFO 02 radiometric record as a function of time. The observed periods can be fitted by exponential function f.

(Fig. 7) (although in the latter case with much larger noise). In comparison with similar cases recorded by the same systems in Central Europe and in Australia, we know that such behavior is typical for type I fireballs

(Ceplecha and McCrosky 1976) as described in detail in Spurný and Ceplecha (2008).

171

The first evident result is that the real maximum of brightness was reached not near the beginning (as suggested from the photographic photometry and discussed above), but during the brightest 0.03 s short flare near the end, at a height of 36.3 km. This maximum of -9.6 absolute meteor magnitudes is about 0.4 magnitudes higher than the photographic maximum at 55.7 km. This difference is caused by the fact that the duration of this flare is much shorter (about one half) than the integration constant of the photographic photometry (see Fig. 10), and that it occurred exactly at the moment when the photographic image was eclipsed by a rotating shutter.

Another evident feature visible only on the photoelectric light curve is periodic changes of the brightness between the heights of 57 and 44 km. The measured times of peaks corresponding to periods cover almost a 2 s long interval (see Fig. 6 or 10), and changes of the frequency range from 9 to 25 Hz as can be seen in Fig. 11. This dependency of the frequency on time can be approximated by an exponential function

$$f = A \cdot (e^{Bt} - 1) + f_0, \tag{1}$$

where A and B are constants and f_0 is an initial frequency. For Bunburra Rockhole, the fit of measured values leads to A = 1.44 and B = 0.99 s⁻¹. When we

extrapolate it into time t=0 we get frequency $f_0=8.4$ Hz, and for t=5.55 s (terminal point) about 700 Hz. However, these values were not observed because of a low s/n ratio near the beginning, and probably other processes involved in light production below a height of 44 km. Nevertheless, if these observed periodic light fluctuations were caused by rotation of the meteoroid, in that case the preatmospheric rotation period would be approximately 8 Hz.

Possible rotation of the meteoroid can be studied from the observed physical parameters. From the fragmentation model analysis (see the Application of the GFM section, Fig. 13), we determined that the first fragmentation point, where the initial body significantly fragmented into several larger pieces, was at a height of 54.9 km when the meteoroid had a speed of 13.20 km s⁻¹. It corresponds to a dynamic pressure of 0.11 MPa, which can be also interpreted as the meteoroid's tensile strength just prior the fragmentation (this is a significantly different value from the strength of the recovered meteorites).

Paddack (1969), Beech (2002), and Beech et al. (2003) presented relationships between the maximum spin rate and material constants of a body (Equations 2 and 3, respectively) resulting from the condition that the centripetal force per unit area is equal to the tensile strength of the meteoroid at the instant of fragmentation.

$$\omega_{\text{max}} = (1/k^*r)\sqrt{(3\sigma/\rho_{\text{d}})}$$
, where $k = \sqrt{(3^*(3 + \mu/8))}$. (2)

$$\omega_{\text{max}} = 1/2r^* \sqrt{(3\sigma/\rho_{\text{d}})}.$$
 (3)

The two relationships are different and provide different results. $\omega_{\rm max}$ is the maximum possible spin rate just before a fragmentation, r is the meteoroid radius at the instant of fragmentation, σ is the meteoroid's tensile strength, $\rho_{\rm d}$ its bulk density, and μ is the Poisson coefficient. When we apply these known values for Bunburra Rockhole (m=22 kg, $\rho_{\rm d}=2700$ kg m⁻³, σ of 0.1 MPa, which is equal to the dynamic pressure at a height of 54.9 km—all these details will be found later in the article), and approximate the meteoroid by a sphere, we obtain a maximum frequency of rotation ($\omega_{\rm max}/2\pi$) of 4.7 Hz (mean value based on Paddack (1969)) and of 7 Hz (based on Beech (2002)), respectively.

The mean value of 4.7 Hz is based on different possible values of the Poisson coefficient μ , which is unknown for Bunburra Rockhole. The Poisson coefficient of a stable, isotropic, linear elastic material cannot be <-1.0 and not >0.5 due to the requirement that Young's modulus, the shear modulus, and bulk modulus have positive values (Gercek 2007). The value of maximum frequency of rotation then falls into the

interval from 4.8 to 4.6 Hz. Most materials have a value of μ ranging from 0 to 0.5, which is in good agreement with the value of 0.3 presented by Paddack (1969) and which corresponds to the maximum frequency of 4.7 Hz. If we compare the two equations we can see that Beech (2002) used k=2, which corresponds to an unrealistic Poisson coefficient of -13.2 (making Equation 3 untrustworthy).

In any case, both values of maximum frequencies resulting from Equations 2 and 3 are significantly smaller than the observed period of changes of brightness in the fragmentation point at 54.9 km. Moreover, they are even smaller than the preatmospheric period of these fluctuations f_0 , i.e., 8.4 Hz. This result is evidently not in agreement with a rotational origin for the periodic changes of the brightness. Either Equations 2 and 3 are not correct or these changes of brightness are not caused by the rotation of the meteoroid. Also, the fact that the changes in brightness are observed prior to and after the fragmentation point at 54.9 km, suggests a nonrotational explanation. A quasi-periodic process during ablation, or involvement of other processes as described in Spurný and Ceplecha (2008), could be more probable explanations of this effect which we observed not only on the Bunburra Rockhole light curve but also on radiometric light curves of many fireballs recorded by the Czech cameras of the European Fireball Network and the DFN as well.

VELOCITY AND THE FRAGMENTATION MODEL ANALYSIS

Input Data and Explanations and Definitions of Used Models

The information about the fireball's velocity is limited, being based only on the data from the DFO 02 image. Thanks to the very good quality of the camera imaging system and the high resolution of the film we were able to measure breaks over almost the entire luminous trajectory, and to get detailed information about velocity and deceleration for all of its atmospheric flight. As can be seen in Fig. 12, we measured a total of 113 breaks (numbered 1-118—three breaks at the beginning [2–4] and two breaks near the end [114 and 115] were not measurable at all), which corresponds to a total duration of 5.7 s. As mentioned earlier in the description of the DFOs, we use a three-blade rotating shutter, which is placed close to the film emulsion, and with a programmed frequency using a step motor providing exactly 21.070 interruptions in 1 s. All input data resulting from the trajectory computation and photographic photometry which were used for the fragmentation model analysis are collected into Table 2,

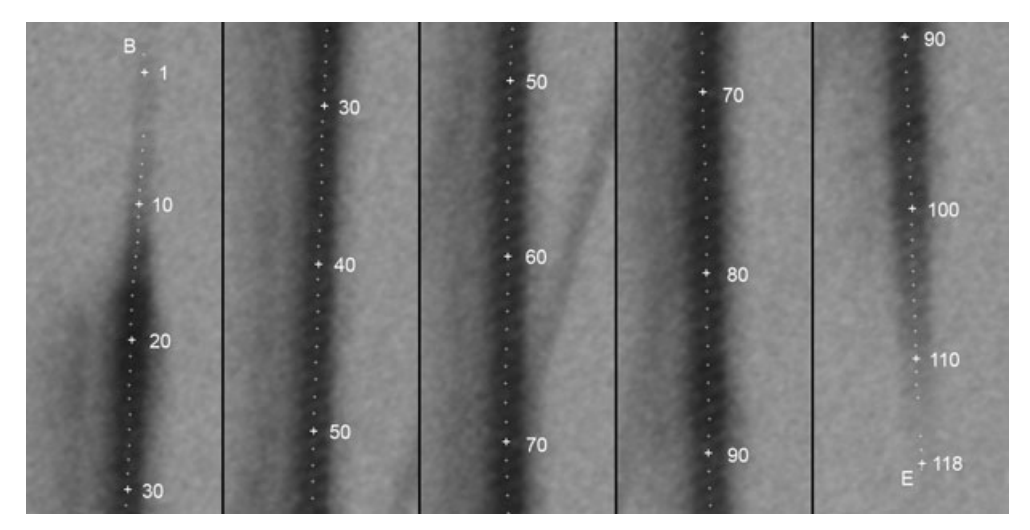


Fig. 12. Detail of the luminous trail of the Bunburra Rockhole fireball on the DFO 02 image showing individual breaks (time marks) as were measured for speed determination.

where time, length, height, and absolute magnitude from photographic photometry (see the Photographic and Photoelectric Photometry section) are given for each measured break. Breaks denoted by an asterisk were not used for the final analysis as is discussed later. These data were used for application of the Gross-Fragmentation Model (GFM) and also the more complex Meteoroid Fragmentation Model (MFM) to provide an overall picture of the fireball's dynamics and fragmentation. At this point, we want to stress that we used photographic magnitudes for MFM analysis because in the DFOs we use films (Ilford FP4) with panchromatic emulsions and our luminous efficiencies are entirely related to the panchromatic pass band.

The term GFM is used for procedures described in Ceplecha et al. (1993). They are based entirely on the dynamical behavior of a meteoroid in the atmosphere. The GFM fits the observed values of height and distance along a trajectory, both as a function of time. However, the GFM does not fit the light curve. The procedure is capable of finding only one fragmentation point (height) inside a given interval and does not involve data on meteor brightness (light curve). The same value of ablation coefficient is assumed before and after the fragmentation point.

The term MFM is used for procedures invented and published by Ceplecha and ReVelle (2005). This model fits both the light curve and height as a function of time (height curve). It involves any number of fragmentation points and two types of fragmentation: (1) into large pieces comparable to the main body in size and (2) into a cluster of very small fragments. The ablation coefficient and the shape–density coefficient are allowed to be variable with height/time. Luminous efficiency is assumed to be variable with velocity, mass, and height

(calibrations were performed mostly by MFM solutions for the Lost City fireball and by masses of the recovered meteorites; Ceplecha 1996). Two limiting assumptions are inevitably demanded in the MFM: (1) the main body is the leading one throughout the entire trajectory, and (2) the luminous efficiency of the main body and of its fragments are identical. The MFM completely explains the differences of dynamically and photometrically determined masses, a puzzle in meteor science for many decades.

The apparent values of the ablation coefficient, σ , and apparent values of the luminous efficiency, τ , are those computed from observational (dynamic and photometric) data of the main body neglecting the fragmentation process.

The intrinsic values of σ and τ are those computed from observational (dynamic and photometric) data of the main body including the fragmentation process.

The intrinsic values of σ and τ are the apparent values corrected for the effect of fragmentation.

Application of the GFM

The basic strategy of the dynamic analysis was the following. First, as given in Table 2, we used the complete data set of observational data on time (t), length (l), height (h), and absolute magnitude (mg) from FishScan photometry at 113 measured time marks (breaks on the image of the fireball) for a preliminary analysis by the GFM (Ceplecha et al. 1993). Note that $l_{\rm obs}$ is used only in GFM analysis whereas in the MFM we work only with observed heights. Both methods take the fireball trajectory as straight, but the relationship between length and height is nonlinear because of the curvature of the Earth. Then we consecutively excluded

Table 2. Observed times, lengths, heights, and absolute magnitudes for each measured break on the Bunburra Rockhole luminous trajectory.

Table 2. *Continued*. Observed times, lengths, heights, and absolute magnitudes for each measured break on the Bunburra Rockhole luminous trajectory.

KOCKIIO	de fullillous	3 2				ourra Nocki	iole fullillious	trajectory.	
$N_{\rm BR}$	T(s)	L(km)	H(km)	Mag.	$N_{\rm BR}$	T(s)	L(km)	H(km)	Mag.
1*	0.0000	0.8908	62.3713	-4.98	57	2.6582	35.847	44.3401	-8.69
5*	0.1899	3.8578	60.8354	-5.11	58	2.7057	36.4584	44.026	-8.72
6*	0.2373	4.6011	60.4508	-4.26	59	2.7532	37.0252	43.7348	-8.65
7*	0.2848	5.2044	60.1387	-4.58	60	2.8006	37.6297	43.4244	-8.67
8*	0.3323	5.8223	59.8191	-4.72	61	2.8481	38.2168	43.1228	-8.64
9*	0.3323	6.4751	59.4814	-4.72	62*	2.8956	38.8548	42.7952	-8.76
10*	0.3797	7.1056	59.1553	- 4 .78	63*	2.943	39.4199	42.7932	-8.70 -8.71
11*	0.4272	7.1030	58.8607	-5.2 -5.71	64*	2.943	40.0084	42.3031	-8.71 -8.53
12*	0.4747	8.28	58.5482	-6.05	65*	3.038	40.6342	41.8817	-8.33 -8.74
13*	0.5696	8.8434	58.2569	-6.5	66*	3.0854	41.2016	41.5905	-8.74 -8.72
14	0.5696	9.4226	57.9576	-0.3 -7.48	67*	3.1329	41.7391	41.3903	-8.72 -8.81
15	0.6645	9.9985	57.6599	-7.44	68*	3.1804	42.3405	41.0061	-8.92
16	0.712	10.6083	57.3448	-8.09	69*	3.2279	42.9254	40.706	-8.85
17	0.7595	11.2324	57.0223	-8.75	70*	3.2753	43.5317	40.3949	-8.94
18	0.8069	11.8523	56.7021	-8.89	71*	3.3228	44.096	40.1055	-9.04
19	0.8544	12.4685	56.3838	-8.96	72*	3.3703	44.5789	39.8579	-8.92
20	0.9019	13.1176	56.0486	-9.17	73*	3.4177	45.1367	39.5718	-8.96
21	0.9494	13.8159	55.688	-9.2	74*	3.4652	45.653	39.3071	-8.95
22	0.9968	14.4042	55.3843	-9.13	75*	3.5127	46.1149	39.0703	-8.78
23	1.0443	14.9885	55.0826	-8.92	76	3.5601	46.6514	38.7953	-9.01
24	1.0918	15.6038	54.765	-8.81	77	3.6076	47.2215	38.5031	-9.04
25	1.1392	16.2859	54.413	-8.79	78	3.6551	47.788	38.2128	-8.96
26	1.1867	16.9282	54.0816	-8.73	79	3.7025	48.3007	37.95	-8.92
27	1.2342	17.5675	53.7517	-8.64	80	3.75	48.8238	37.682	-8.85
28	1.2816	18.1506	53.4509	-8.64	81	3.7975	49.3555	37.4096	-8.77
29	1.3291	18.7304	53.1518	-8.45	82	3.845	49.8477	37.1575	-8.74
30	1.3766	19.3749	52.8194	-8.55	83	3.8924	50.385	36.8823	-8.76
31	1.424	20.031	52.4811	-8.46	84	3.9399	50.8968	36.6202	-8.71
32	1.4715	20.6168	52.179	-8.45	85	3.9874	51.4285	36.3479	-8.96
33*	1.519	21.1336	51.9126	-8.3	86	4.0348	51.9216	36.0955	-8.84
34*	1.5664	21.7462	51.5969	-8.41	87	4.0823	52.3999	35.8506	-8.89
35	1.6139	22.4051	51.2573	-8.52	88	4.1298	52.9003	35.5945	-8.85
36	1.6614	23.0263	50.9371	-8.5	89	4.1772	53.3839	35.3469	-8.52
37	1.7088	23.66	50.6107	-8.37	90	4.2247	53.8649	35.1007	-8.37
38	1.7563	24.2884	50.2869	-8.49	91	4.2722	54.3453	34.8549	-8.33
39	1.8038	24.8973	49.9732	-8.33	92	4.3196	54.7881	34.6283	-8.25
40	1.8512	25.551	49.6365	-8.38	93	4.3671	55.2403	34.397	-8.15
41	1.8987	26.1369	49.3349	-8.35	94	4.4146	55.6677	34.1783	-8.06
42	1.9462	26.7198	49.0347	-8.51	95	4.4621	56.1378	33.9379	-8.49
43	1.9937	27.315	48.7283	-8.52	96	4.5095	56.594	33.7046	-8.15
44	2.0411	27.9522	48.4003	-8.57	97	4.557	57.0484	33.4721	-7.75
45	2.0886	28.6162	48.0585	-8.62	98	4.6045	57.5112	33.2355	-7.86
46	2.1361	29.1987	47.7587	-8.45	99	4.6519	57.9278	33.0225	-7.8
47	2.1835	29.7942	47.4523	-8.5	100	4.6994	58.308	32.8281	-7.47
48	2.231	30.4451	47.1174	-8.61	101	4.7469	58.7195	32.6177	-7.31
49	2.2785	31.0469	46.8079	-8.54	102	4.7943	59.1074	32.4194	-6.93
50	2.3259	31.6462	46.4997	-8.66	103	4.8418	59.5151	32.2111	-6.7
51	2.3734	32.2995	46.1637	-8.68	104	4.8893	59.8892	32.0199	-6.48
52	2.4209	32.8755	45.8675	-8.68	105	4.9367	60.239	31.8411	-6.15
53	2.4683	33.4193	45.5879	-8.57	106	4.9842	60.6202	31.6463	-5.79
54	2.5158	34.0033	45.2877	-8.59	107	5.0317	61.0005	31.452	-5.72
55	2.5633	34.6406	44.9601	-8.8	107	5.0791	61.3676	31.2645	-5.72 -5.31
56	2.6107	35.2027	44.6712	-8.66	108	5.1266	61.7223	31.2043	-3.31 -4.99
50	2.0107	33.4041	77.0/14	-0.00	107	3.1200	01.7223	31.0034	7.22

Table 2. *Continued*. Observed times, lengths, heights, and absolute magnitudes for each measured break on the Bunburra Rockhole luminous trajectory.

$N_{\rm BR}$	T(s)	L (km)	H (km)	Mag.
110	5.1741	62.0432	30.9193	-4.53
111	5.2215	62.3637	30.7556	-4.2
112	5.269	62.6823	30.5929	-4.42
113	5.3165	62.9805	30.4406	-3.83
116	5.4589	63.8662	29.9883	-3.48
117	5.5064	64.1905	29.8227	-2.72
118	5.5538	64.5136	29.6577	-2.72

values with large and systematic deviations, which meant that in the final set 87 values left for the final grossfragmentation solution and for the MFM analysis. The discarded points were as follows: (1) during the trajectory beginning from 62.4 to 58.2 km height; (2) two points at 51.9 and 51.6 km height; and (3) during a significant part of the trajectory from 42.8 to 39.1 km height. These rather severe deviation anomalies might be caused by enormous fragmentation at the trajectory beginning and by different large fragments forming the head of the phenomenon around 40 km height. We applied MSISE90 (Hedin 1991) model of atmospheric densities, however, adapted to realistic atmospheric densities of the event below 30 km height used by those for the calculation of the dark flight (will be explained later in the Darkflight and Prediction of the Impact Area section). These air densities were about 9% higher against the MSISE90 values. Time and distance along the trajectory are relative values; thus we have chosen as a zero point (from where the integration starts) a height somewhat above the observed beginning point, i.e., t = 0 was set at h = 65.0 km, which is slightly higher than the first observing point on the luminous trajectory at an altitude of 62.83 km (see Table 1).

A single-body solution was found for these 87 points as the only existing realistic gross-fragmentation solution. This solution is described by the following parameters:

 $\sigma_a = 0.0331 \pm 0.0007 \text{ s}^2 \text{ km}^{-2}$ (σ_a is the apparent value of the ablation coefficient, i.e., including

fragmentation), $\varepsilon_{\rm l}=\pm 15$ m, $h_1=57.96$ km, $v_1=13.224\pm0.003$ km s⁻¹, $m_1=22.1\pm0.3$ kg (dynamic mass), and $m_{\rm E}=1.5\pm0.2$ kg (dynamic mass). Subscript 1 indicates data for the first measured point in the corrected input data (i.e., corresponding to h_1).

The GFM, which resulted in only the single-body solution, can fully explain the motion of the Bunburra Rockhole fireball, when these 87 selected points are used. The large average apparent value of the ablation coefficient explains the motion of the body with quite good precision. However, heights as a function of time without the omitted parts of the trajectory are far outside this single-body solution, making the standard deviation dependent on time. It was also the motivation for using the more complex MFM.

Application of the MFM

Observational data on the 87 selected points as mentioned in the previous section were analyzed by the MFM after application of the GFM. The resulting shape–density coefficient K changed significantly with height (Table 3). The solution also yielded somewhat lower values of intrinsic σ , which stayed constant during the entire trajectory and was equal to $0.002 \, \mathrm{s^2 \, km^{-2}}$ with standard deviation limits 0.001–0.004. The MFM solution needed severe gross-fragmentation into comparable larger fragments at a height of 54.9 km. All attempts to avoid this scenario proved unsuccessful.

The resulting initial mass from MFM is 22 kg and is identical with the gross-fragmentation solution as shown in the Application of the GFM section. With known bulk density of BR meteorites of 2700 kg m⁻³ and with an assumption of a spherical shape, it corresponds to a diameter for the original meteoroid of 25 cm, i.e., approximately the size of the football. It is in a good agreement with the result based on analysis of cosmogenic radionuclides and noble gases (Welten et al. 2011) where the most probable value is 20–30 cm.

With application of the MFM, we were able fully to explain height as a function of time (height curve)

Table 3. The most significant fragmentation events for the Bunburra Rockhole fireball resulting from the Meteoroid Fragmentation Model (all entries are described in the Application of the MFM section).

$h_{\rm f}({\rm km})$	$V_{\rm f}({\rm km~s}^{-1})$	$(dv/dt)_f$ (km s ⁻¹)	$\Delta m_{\rm p}$ (%)	$\Delta m_{\rm F}$ (kg)	m (kg)	K (cgs)	$\sigma (km^2 s^{-2})$	Δm_{LP} (%)	p _d (MPa)
$62.83 (h_{\rm B})$	13.310	0	_	_	22.0	0.20	0.001	_	_
54.9	13.194	-0.26	60	12.92	21.5	0.90	0.002	92	0.11
37.8	11.262	-2.20	28	1.53	5.5	0.50	0.002	0 0.74	
37.3	11.036	-2.56	10	0.39	3.9	0.40	0.002	0	0.77
35.85	10.441	-2.57	46	1.59	3.5	0.40	0.002	0	0.85
33.6	9.14	-2.87	10	0.17	1.7	0.35	0.002	0	0.90
31.3	7.61	-2.44	10	0.14	1.4	0.28	0.002	0	0.89
$29.59 (h_{\rm E})$	5.77	-2.44	_	_	1.1	0.35	0.002	_	_

together with the observed light curve of the Bunburra Rockhole fireball with the following values:

 $\sigma = 0.002 \text{ s}^2 \text{ km}^{-2} \text{ standard deviation limits are from}$ 0.001 to 0.004, $\varepsilon_h = \pm 15$ m, where ε_h is the standard deviation for one measured height, K = 0.2-0.9 cgs (K is a function of time). Integration started $(t_1 = 0 \text{ s})$ at $h_1 = 65.0 \text{ km with } v_1 = 13.313 \pm 0.007 \text{ km s}^{-1}, z_B =$ 58.78°, $m_1 = 22.0 \pm 1.3$ kg, and terminated in time $t_{\rm E} = 5.98 \text{ s}$ at height $h_{\rm E} = 29.59 \text{ km}$ with $v_{\rm E} = 5.77 \pm 0.04 \text{ km s}^{-1}$ and $(dv/dt)_{\rm E} = -2.44 \pm 0.05 \text{ km s}^{-2}$, which results in $m_E = 1.1 \text{ kg}$ (meteoroid density 2700 kg m⁻³; standard deviation limits from 0.7 to 1.7). The light curve fit was obtained with a precision of $\varepsilon_{\rm M} = \pm 0.32$ magnitudes, where ε_M is the standard deviation for one measured brightness in stellar magnitudes. Note that the standard deviation for velocity determination describes the precision of the mathematical fit of observed values in the MFM. For the preatmospheric velocity, which is important for computation of the heliocentric orbit, we used a more conservative value of ± 0.015 km s⁻¹, which better reflects the spread of directly measured values. The preatmospheric velocity was computed from our model by extrapolating the observed velocity to the height of the negligible atmospheric density (150 km). The final value of the preatmospheric velocity is $v_{\infty} = 13.365 \pm 10$ 0.015 km s^{-1} .

The resulting values of $v_{\rm f}$, $({\rm d}v/{\rm d}t)_{\rm f}$, σ (intrinsic), and K, together with the heights, amounts of fragmentation for the most important fragmentation points, and corresponding dynamic pressure $p_{\rm d}$, are collected in Table 3. Individual entries have the following meaning: $h_{\rm f}$ is the height of the gross-fragmentation point (the start of the flare), $\Delta m_{\rm p}$ is mass loss at this height in the form of fragments, expressed in percents of the instantaneous mass of the main body m, $\Delta m_{\rm F}$ is the total mass fragmented at the given fragmentation point in kilograms, and $\Delta m_{\rm LP}$ is the part of $\Delta m_{\rm p}$ fragmented as large fragments expressed in percents of $\Delta m_{\rm p}$.

The general scenario of the fragmentation history of the BR fireball is presented in Fig. 13 where a plot of the mass loss against observed heights is shown. Excepting many smaller fragmentations where only a small amount of mass fragmented solely in clusters of tiny fragments which were very quickly ablated (necessary for the exact fit of the observed light curve), there were about six significant fragmentation events as it is listed in detail in Table 3. The most significant fragmentation occurred near the beginning at a height of 54.9 km where the initial meteoroid fragmented into large pieces (no similar fragmentation occurred later during its flight). This fragmentation proved necessary for fitting the observed light curve. In other words, we can interpret this fragmentation scenario that in form of surviving mass, i.e., meteorites, we can expect one main piece which

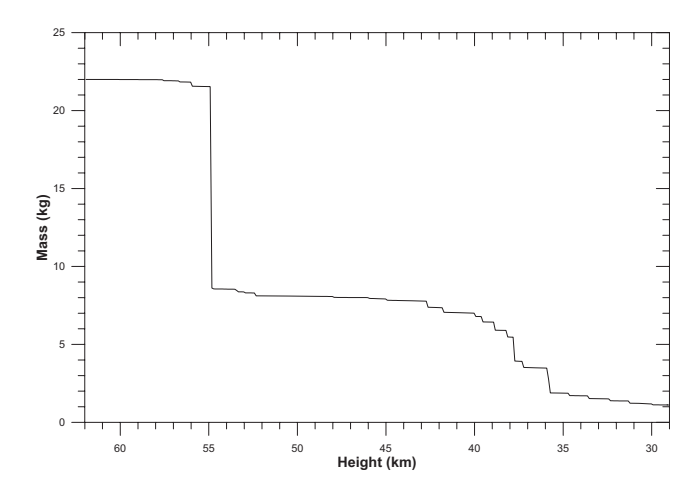


Fig. 13. The computed mass of the main body as resulted from the Meteoroid Fragmentation Model of the Bunburra Rockhole fireball. The most significant fragmentations occurred at a height of 54.9 km (60% of a mass before fragmentation), 37.8 km (28%), and 35.85 km (46%) (see Table 3).

could be in the best case about 1 kg (if not fragmented after the ablation phase), very probably several smaller (hundred grams) pieces which resulted from high altitude fragmentation, and dozens of smaller fragments originating from fragmentation points near the end of trajectory.

In some parameters, such as velocity profile and initial mass, the MFM solution is almost identical with the gross-fragmentation solution, proving the assumption used for omitting quite a large number of original data to increase the precision and reliability of the result. This is an addition to the main proof: recovering meteorites at the predicted locations with predicted masses (see the Darkflight and Prediction of the Impact Area section). Using the selected 87 points, MFM fits the height as a function of time (Fig. 14) and the light curve (Fig. 15) with the precision of the observations. If the MFM solution for the 87 selected points is applied to all 113 points and the residuals of heights are visualized as a function of height (Fig. 16), the enormous values at the beginning may be explained by gross-fragmentation into larger fragments already above 60 km height under quite a low aerodynamic pressure (Spurný and Ceplecha 2008). The trajectory part between 42.8 and 39.1 km with large systematic residuals of height can perhaps best be explained by large fragments exchanging the leading position (different fragments formed the head of the phenomenon during these heights).

RADIANT AND HELIOCENTRIC ORBIT

From the exact time of the fireball passage, its initial velocity, and the position of the apparent radiant, we

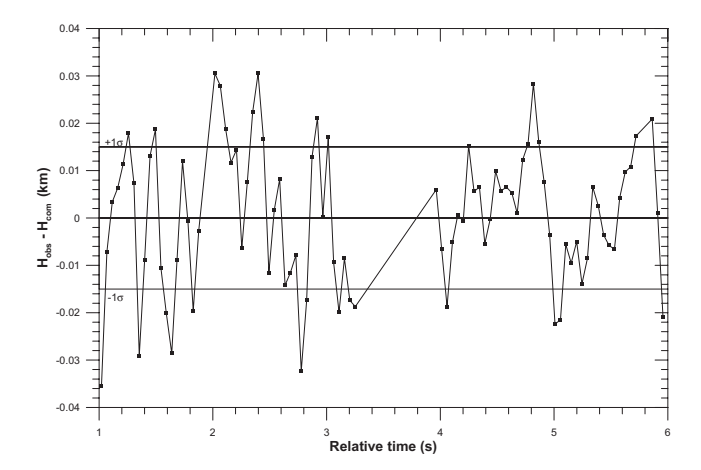


Fig. 14. Residuals of heights of the Meteoroid Fragmentation Model fit to the observed heights as a function of time of the Bunburra Rockhole fireball.

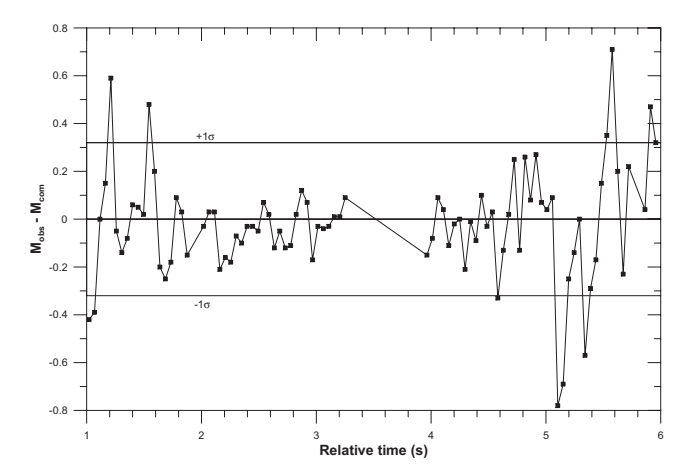


Fig. 15. Residuals of magnitudes of the Meteoroid Fragmentation Model fit to the photographic light curve as a function of time of the Bunburra Rockhole fireball.

computed the heliocentric orbit using the procedure described in Ceplecha (1987). Usually, these input parameters are determined with different precision and reliability. In the case of the Bunburra Rockhole fireball, we know all these values with high reliability, which makes the orbit of the BR one of the most precise of all instrumentally recorded meteorite falls.

The time of the fireball passage is known very precisely from the brightness sensor placed in each AFO as was discussed in the Photographic and Photoelectric Photometry section. DFOs at each DN station are continuously corrected through direct Internet connection with a time server. As mentioned above we recorded the light curve of the BR fireball by two independent DFOs with a time resolution of 2 ms, and because we were able to identify a very sharp maximum flare on each record we determined its absolute time as $19^h13^m57.32^s \pm$

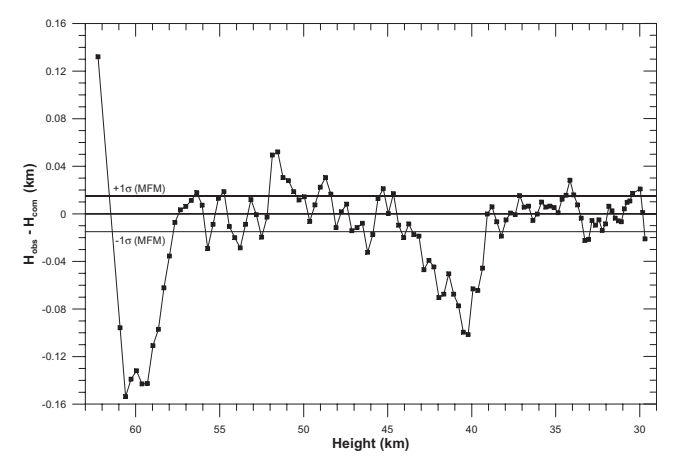


Fig. 16. Residuals of heights of the Meteoroid Fragmentation Model solution for the 87 selected points as it is applied to all 113 measured points.

Table 4. Radiant and orbital elements (J2000.0) of the Bunburra Rockhole meteorite fall (time is given for the photographic beginning of the fireball).

Time (UT)	$19^{\rm h}13^{\rm m}53.24^{\rm s}~\pm~0.05^{\rm s}$
α_{R} (°)	62.62 ± 0.03
δ_{R} (°)	-22.59 ± 0.03
$v_{\infty} (\mathrm{km \ s^{-1}})$	13.365 ± 0.007
α_{G} (°)	80.73 ± 0.06
δ_{G} (°)	-14.21 ± 0.04
$v_{\rm G}~({\rm km~s}^{-1})$	6.743 ± 0.014
$v_{\rm H}~({\rm km~s^{-1}})$	26.659 ± 0.008
a (AU)	0.8529 ± 0.0004
e	0.2427 ± 0.0005
q(AU)	0.6459 ± 0.0007
Q(AU)	1.05991 ± 0.00011
ω (°)	210.04 ± 0.06
Ω (°)	297.595
i (°)	8.95 ± 0.03
P (years)	0.7877 ± 0.0005

0.01^s UT. For determination of the heliocentric orbit, we took the time of the average point on the luminous trajectory where we corrected the observed velocity vector for the Earth's rotation. The meteoroid was in this point exactly at 19^h13^m56.13^s UT. Coordinates of this point are defined by geographic longitude of 129.49510° E, geographic latitude of -31.40427° S, and height of 43.424 km. The speed of the meteoroid at this point was 12.374 km s⁻¹ and the direction of this velocity vector is defined by the apparent radiant position which is expressed by right ascension of 62.704° and declination of -22.568°. These values can be useful for backward orbital integration.

The resulting heliocentric orbit of the Bunburra Rockhole meteoroid (given in the J2000.0 equinox) is defined by the individual elements collected in Table 4

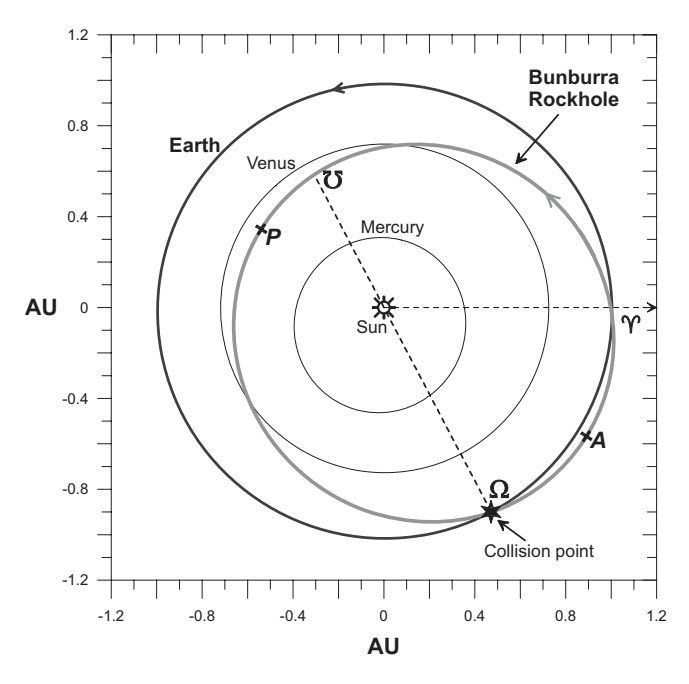


Fig. 17. Orbit of the Bunburra Rockhole (BR) (thick gray line) projected on the plane of the ecliptic, with orbits of Earth, Venus, and Mercury. P and A denote the positions of perihelion and aphelion, respectively, of the BR orbit; Ω and ∇ are the ascending and descending nodes and the dashed line connecting them is the nodal line dividing part of the orbit above (right side) and below (left side) the ecliptic plane; Υ indicates the direction to the vernal equinox.

and it is also plotted as a projection onto the ecliptic plane in Fig. 17. These elements differ slightly from those that we already published in Bland et al. (2009, 2012). This difference is caused by the change of initial velocity as resulted from the MFM (see the Application of the MFM section) mostly because we used the different model of atmospheric densities (modified MSISE90 instead of CIRA72 used in original computations). All orbital elements shown in Table 4 are accompanied by their standard deviations. Obviously, the BR orbit is one of the most precise orbits ever calculated for a meteorite dropping fireball.

The very interesting and unusual feature of the BR orbit is that its semimajor axis is significantly smaller than 1 AU and that virtually the entire orbit was contained within Earth's orbit. It is an Aten type orbit which is very rare among the fireballs with reliably determined orbits. It also means that it significantly differs in character from all meteorites with known orbit because all these bodies orbited the Sun on the Apollo type orbits with their aphelion distances deeply inside the Main Belt of asteroids. By contrast, the BR meteoroid collided with Earth practically in its aphelion and orbited the Sun only once per 287 days. However, such a short orbit is very chaotic and it is very difficult to trace the BR orbital

history deeply backward because there were many close approaches with Venus and Earth quite recently (Bland et al. 2009). Nevertheless, as it was shown in Bland et al. (2009), modeling of the BR orbital history indicates that it originated with a very high probability of 98% from the innermost Main Belt and there is a 72% probability that it was delivered from the ν_6 resonance. From the meteorite analysis combined with the orbital studies the BR parent body would likely be classified as a V-type asteroid, but from a parent body other than the asteroid 4 Vesta, which is widely accepted as a source of the great majority of basaltic meteorites, especially eucrites.

At the time of the BR meteorite fall and the meteorite's recovery, it was only the tenth such case with the reliably determined heliocentric orbit based on instrumental data; the first case an Aten type orbit; and the first orbit for another type of meteorite other than a chondrite.

DARKFLIGHT AND PREDICTION OF THE IMPACT AREA

Basic information about the BR darkflight was already mentioned in Spurný et al. (2009) and Bland et al. (2012). Here, we present more details how we modeled the darkflight and impact area.

The computation of the darkflight, and determination of the impact position of possible meteorites, was complicated by the fact that the terminal height (where we had the last definitive information about meteoroid position and velocity vector) was relatively high—almost 30 km above the surface. Such a high terminal height translates into about 6 min of the darkflight for a 100 g meteorite, in contrast to only a 6 s duration of the recorded luminous trajectory. It was a great challenge to model the BR darkflight because the vast majority of previously recovered cases were deeply penetrating fireballs with terminal heights below or around 20 km. and with much larger predicted terminal masses. There was only one exception, the Tagish Lake meteorite fall, which also terminated above or around 30 km. However, the initial mass of this body was at least about three orders of magnitude higher than the BR mass. In addition to a very high terminal point, our situation was still more complicated by very strong stratospheric winds up to 50 m s⁻¹. Such speed is comparable with the free fall speed of the penetrating meteoroid of similar size which was found. It is evident that such atmospheric conditions highly affected the final position of the landing meteorites.

The final complication we met in this stage of the darkflight modeling was the fact that we had at our disposal three independent data sets for high altitude winds, which resulted in not negligibly different positions

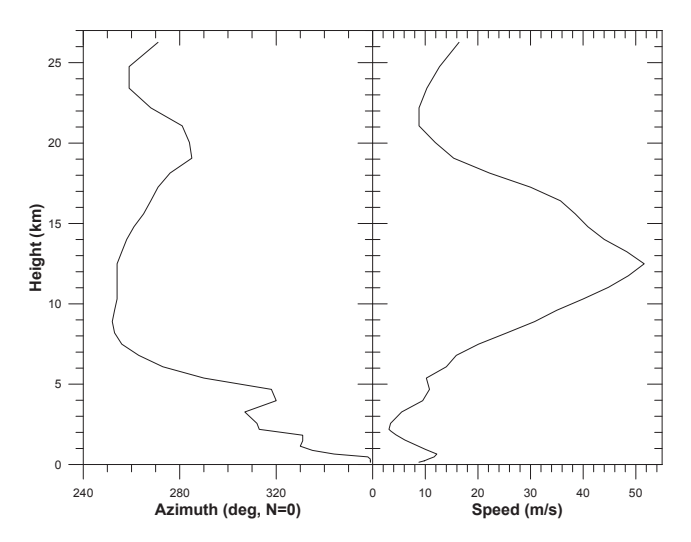


Fig. 18. Vertical profile of atmospheric wind azimuth and speed used for Bunburra Rockhole dark flight computation. This profile is based on Imperial College implementation of the Weather Research and Forecasting model and corrected by directly measured balloon data from Eucla station (source: Imperial College London and University of Wyoming).

for the impact area. This difference for the modeled mass range (1 kg-1 g) was up to several hundred meters. From this reason we had first to decide which model seemed to be best for this purpose, and take that model for the final darkflight computation. We tested the following wind models:

- (a) Direct balloon measurements taken every GMT midnight from the station Eucla, which is on the southern edge of the Nullarbor and which was only several tens of kilometers away from the terminal point of the BR trajectory.
- (b) Global UKMO wind model data.
- (c) Version 3 of the Weather Research and Forecasting (WRF) model (Skamarock et al. 2008), provided by Imperial College London for the given place and time.
- (d) Combination of the variant (a) and (c), i.e., modified IC WRF model nudged toward observed atmospheric profiles from available Eucla balloon data.

After critical evaluation of all possibilities we took the variant (d) where we used two direct balloon measurements from Eucla station (before and after the event) and included them into the Imperial College implementation of the WRF model of the Earth's atmosphere. As a result we got the atmospheric profile which contains pressure, temperature, and wind speed and direction for the whole range of heights covering darkflight and for the time and position of the event. Resulting values of the wind speed and wind direction as dependent on height are shown in Fig. 18.

For BR darkflight computations, we used the procedure described in Ceplecha (1987). We started darkflight computation at a height of 27 km where the meteoroid speed decreased below 3 km s⁻¹, which is usually taken as the ablation limit. As was shown in the Velocity and the Fragmentation Model Analysis section where fragmentation of an initial meteoroid was discussed. it significantly fragmented during its atmospheric flight. Therefore, we can expect that at least several pieces with masses ranging from several grams to hundreds of grams could land on the ground. Using the wind profile, positional information of the terminal point, and observed values of velocity and deceleration (discussed above) extrapolated to 27 km, we could model the darkflight and compute the impact position for the meteorites. We repeated it for different masses ranging from 1 kg to 10 g to obtain positions of individual impact points. Individual pieces moved down to the surface on very complicated trajectories as it is shown for five different masses in Figs. 19a-c. Figure 19a shows the motion of meteorites from the top view and we can see that pieces were shifted by wind according to their masses in the range from 2 km for a 1 kg meteorite to almost 10 km for a 10 g meteorite in comparison with positions for meteorites of the same size without the effect of wind taken into account. This shift for meteorite masses of about 100 g was about 7.6 km. As a result of this darkflight modeling, we arrived at the highest probability line where the meteorites could be found. This result was not very encouraging because the length of the predicted impact area, as a result of the relatively low inclined trajectory and strong wind influence, for possible masses of meteorites ranging from 1 kg to 10 g, was about 12 km. This situation is illustrated in Fig. 20, where the highest probability line with impact points for different masses and positions of recovered meteorites is schematically shown.

SEARCHING FOR METEORITES AND THEIR RECOVERY

The predicted impact area was on territory of Southern Australia (see Figs. 8 and 20) in the eastern part of the Nullarbor Plains. As was shown above (in the Application of the MFM section) we could expect one larger 1 kg piece, a few smaller pieces of about one hundred of grams, and dozens of small 1–10 g pieces resulting from three fragmentation events near the end of luminous trajectory. Such a scenario resulted in a very elongated—at least 12 km long—area. It was unrealistic to search such a large area systematically, so our searching strategy was focused close around the line of the highest probability with only a few hundred meter long transverse scans and we searched in such mass limits where the fall and find were the most probable (i.e.,

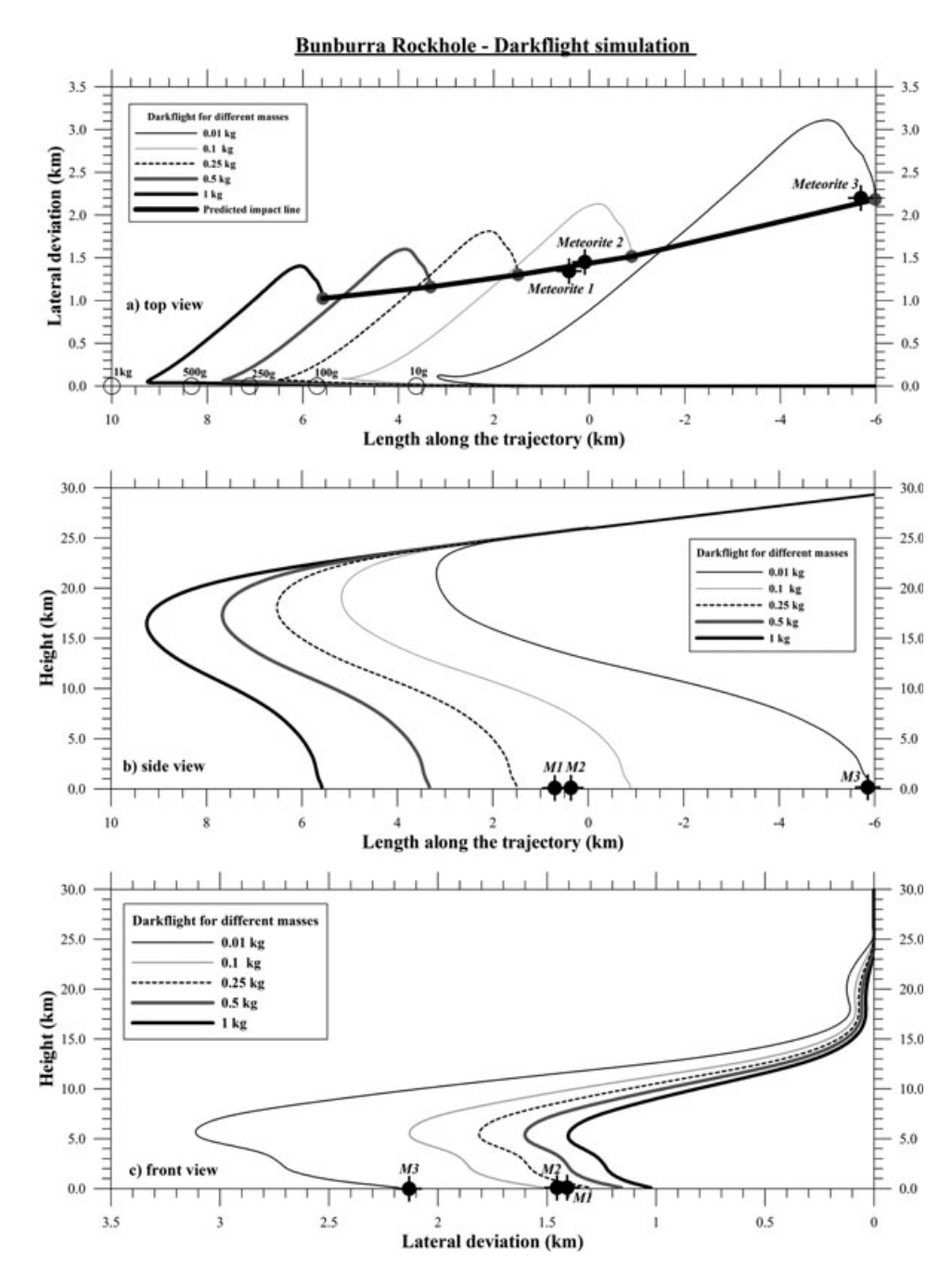


Fig. 19 a–c) Dark flight simulation for different masses of meteorites for top, side, and front perspectives and positions of all three recovered meteorites. Empty circles in the plot (a) are computed positions of the meteorites for different masses without action of the wind. Corresponding filled circles represent impact positions including the effects of wind and they define the most probable impact line. The distance between these positions grows from about 2.5 km for the hypothetic 1 kg piece to more than 10 km for a 10 g piece. It is 7.6 km for the recovered meteorites 1 and 2. Agreement of theoretical model with positions of recovered meteorites is excellent and completely confirmed all our assumptions.

combination of possible size and number of expected pieces). It was the reason why we decided to start the search in the area of hundreds of grams, strictly speaking in the area from 100 to 250 g as shown in Fig. 20.

We organized a first searching trip in October 2008. However already 1 yr before, when we were on a servicing trip around the stations in November 2007, and knew preliminary position of the BR impact area, we were able to conduct a survey flight with a light aircraft to get direct information about the impact area, i.e., to know which kind of vegetation was there and how we could reach it by vehicles. It fulfilled our expectations

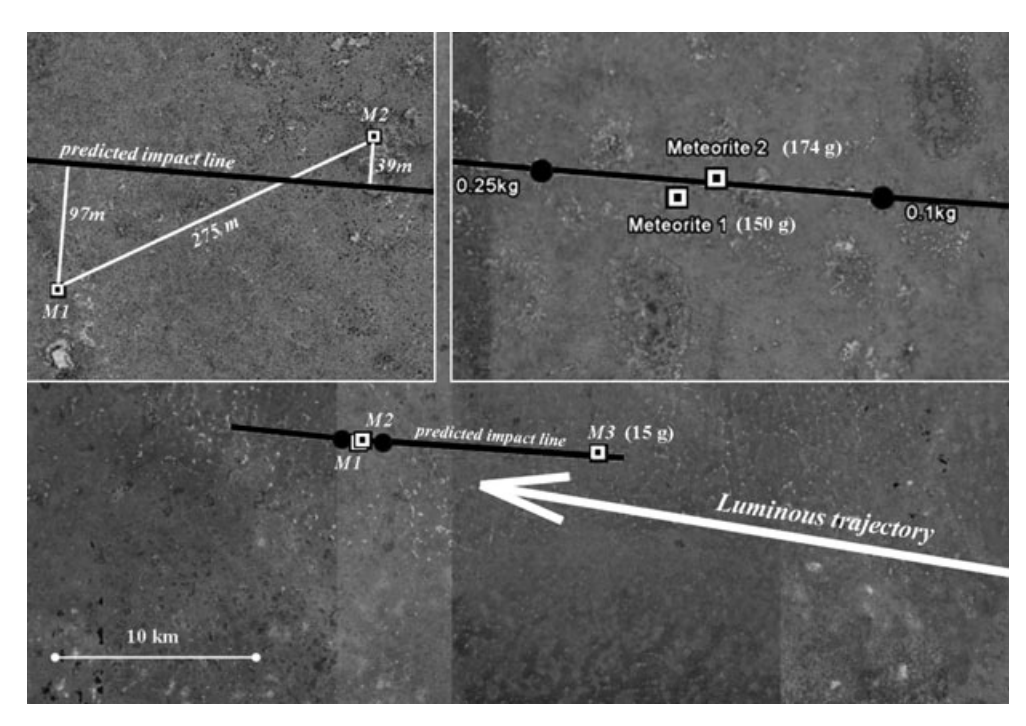


Fig. 20. Situation map with end of the fireball (white arrow), predicted impact line (black), and the position of the recovered meteorites (black and white squares). It documents an excellent agreement of the prediction with reality.



Fig. 21. Members of the first Bunburra Rockhole (BR) searching trip. Starting from the left: Clive Daw (finder of the BR1 meteorite), David Vaughan, Martin Towner, Phil Bland (finder of the BR2 meteorite), Pavel Spurný (holding BR1 meteorite), Graham Kennedy, Trudi Kennedy, and Pavel Trepka.

and we got very worthwhile information, which helped us with effective organization of the searching trip in 2008. We were a small group of eight people (Fig. 21) and for this expedition we used one truck, three 4WD cars, and two quad bikes (transported to the area by truck). The vast majority of the impact area was covered by open bush up to 1 m height with only small spots completely without vegetation (see Fig. 22). We set up the base camp in the area of 100 g and we searched this most probable area systematically by two main



Fig. 22. Aerial view of the Bunburra Rockhole impact area from the inspection flight on November 20, 2007. The area is covered by a low sparse bush around numerous spots without vegetation.

ways—from quad bikes and by foot. The reality exceeded all our expectations. The first meteorite with mass of 150 g was found from a quad bike only 97 m southward from the highest probability line, and it was found at the end of the first searching day of this first searching trip. It was on October 3, 2008 at 5:15 p.m. local time (WST). The meteorite had a complete fusion crust of glazy black color and was easily visible on the surface from a distance of several meters. The second meteorite with mass of 174 g was recovered on October

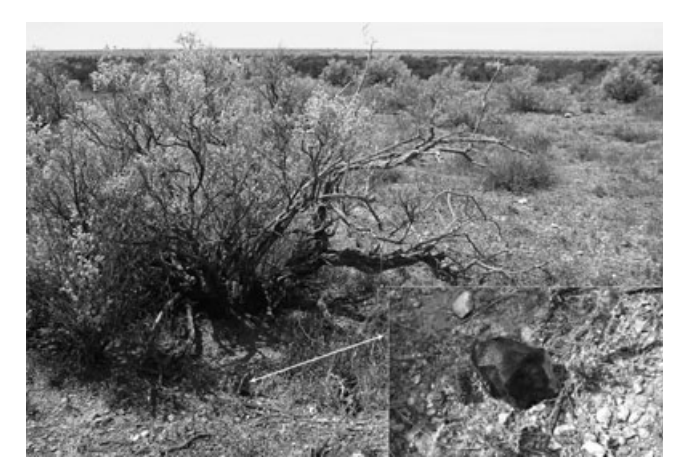


Fig. 23. The finding place of the second Bunburra Rockhole meteorite with the meteorite in the finding position.



Fig. 24. The Bunburra Rockhole meteorites 1 (right) and 2 (left) found during the first searching expedition.

11, 2008 at 11:08 A.M. local time. It was found only 39 m northward from the central line in a small area which was left unsearched until the last searching day. We found it by foot and in contrast to the first piece, this meteorite was broken and a small part (about 20%) of it was missing and was not found in the local area. This meteorite and the impact area around the finding position are shown in Fig. 23. The distance between meteorites was 275 m. It is well documented in Fig. 20

where comparison of the prediction with real position of the recovered meteorites is shown. Both meteorites found during this expedition looked very fresh although they spent more than 14 months in the desert. They are shown in Fig. 24. In February 2009, during the next searching trip, a third meteorite of only 15 g mass was found. It was recovered again <100 m from the highest probability line in the area of corresponding masses (10 g area), and it had a complete fusion crust similar to the first meteorite. Some details about all three recovered Bunburra Rockhole meteorites are collected in Table 5. We also searched systematically in the area of 1 kg piece but without success. This is likely due to the large fragment breaking into smaller pieces after the ablation phase.

The meteorites were recovered not far from the landscape structure named Bunburra Rockhole, so this fall and meteorites were named after it—the Bunburra Rockhole. Detailed description of the meteorite, classified as an anomalous basaltic eucrite, is given in Bland et al. (2009) and other meteorite analyses are published in Benedix et al. (2010), Towner et al. (2010), Spivak-Birndorf et al. (2010), Welten et al. (2011), and Bland et al. (2012).

This successful recovery exactly in the predicted impact area proved the correctness of our observational and computational methods and models.

DISCUSSION

The Bunburra Rockhole meteorite fall has several important primacies and this result is exceptional from many aspects. First of all, the Bunburra Rockhole is one of the most precisely described meteorite falls in history, and this observation is still valid 4 yr after the fall when we know of seven new instrumentally documented falls: Almahata Sitta (Jenniskens et al. 2009), Buzzard Coulee (Hildebrand et al. 2009), Jesenice (Spurný et al. 2010), Grimsby (Brown et al. 2011), Košice (Borovička et al. personal communication), Mason Gully (Spurný et al. 2011; Towner et al. 2011) and recently (February 4, 2011) Križevci meteorite fall in Croatia recorded by Croatian and Slovenian Meteor Network and European Fireball Network.

Bunburra Rockhole is the fifth predicted meteorite fall in history, i.e., that the meteorites were found on the

Table 5. Details of recovered meteorites.

		Coordinates				
Meteorite	Mass (g)	Longitude (E)	Latitude (S)	Altitude (m)	Date of recovery	Finder
M1	150	129.188°	-31.350°	119	October 3, 2008	Clive Daw
M2	174	129.190°	-31.349°	118	October 11, 2008	Phil Bland
M3	14.9	129.320°	-31.355°	113	February 27, 2009	Tony Davies

basis of previous analysis of the instrumental records. BR was a successor to such exceptional cases as Příbram (Ceplecha 1961), Lost City (McCrosky et al. 1971), Innisfree (Halliday et al. 1978), and Neuschwanstein (Spurný et al. 2003). All remaining instrumentally recorded meteorite falls were found independently on the following data analysis (Peekskill, Brown et al. 1994; Tagish Lake, Brown et al. 2000; Morávka, Borovička et al. 2003; Park Forest, Brown et al. 2004; and Villalbeto de la Pena, Trigo-Rodríguez et al. 2006). As was shown in the Searching for Meteorites and Their Recovery section, in the case of BR fall the prediction was very precise and the recovery of three meteorites exactly in the predicted area in the predicted mass range completely proved not only our dark flight modeling but also all atmospheric trajectory analysis. Although these data are usually not published, we suggest that BR was the most precisely predicted meteorite fall so far.

Another interesting aspect of the Rockhole meteorite fall is that it is the first case from all instrumentally recorded falls which was observed only by dedicated instruments and all presented results are based only on analysis of these data. There was no casual visual observation reported because the fireball flew over remote and completely uninhabited areas of the Nullarbor Plain. Due to the relative faintness of this event, it was also not recorded by any global observing system such as ground-based infrasound and seismic networks, and also by satellites from space. So, without our unique experiment this fall would be completely unknown. It is also the first meteorite recovery based on data from the new instrument which we developed for the purpose of fireball observations—AFO/DFO. BR is the first instrumentally observed meteorite fall in the southern hemisphere, which means also in Australia. And finally, it is the first documented meteorite fall from a relatively small meteoroid, which produced only a moderate brightness fireball with a terminal height of 30 km. All previous observed meteorite falls were caused by much larger bodies which produced much more spectacular bolides and, with the exception of the Tagish Lake fall, they penetrated much deeper in the atmosphere and terminated at heights around or even below 20 km.

The heliocentric orbit of the BR is also very exceptional, as it is the first known meteorite from an Aten type orbit, and BR is the first meteorite classified as an achondrite with a known orbit. Moreover, due to its distinct oxygen isotope composition, it is classified as an ungrouped achondrite similar in mineralogical and chemical composition to eucrites but with origin in a different parent body than the asteroid Vesta (Bland et al. 2009). The BR orbital history indicates that it originated with a very high probability of 98% from the

innermost Main Belt, and there is a 72% probability that it was delivered from the v_6 resonance. The BR heliocentric orbit is one of the most precise orbits ever calculated for a meteorite dropping fireball.

From detailed light curve taken by the DFO fast photometer, we revealed that periodic changes which are visible in the first half of the BR luminous trajectory are likely not caused by rotation of the original meteoroid because frequency of these changes is much higher than expected based on the tensile strength of the meteoroid which resulted from fragmentation history given by fragmentation model. The exact explanation of this observed behavior (which we have known for some time based on radiometric light curves of many similar fireballs observed by the same technique from the Czech part of the European Fireball Network) remains unclear.

The important result from the fragmentation model analysis is that the Bunburra Rockhole meteoroid was approximately 25 cm on diameter with a rather weak structure as it underwent several fragmentations during its atmospheric flight under relatively small dynamic pressures.

The Bunburra Rockhole meteorite fall clearly proved and justified our methodological approach that only high resolution observations could yield such good impact position data, even for a relatively unfavorable case.

Our general conclusion resulting from the Bunburra Rockhole fall is that this project in the remote and hostile environment of the Australian desert is meaningful, and that these observations can bring data of fundamental value to solar system research.

Acknowledgments—This work was supported by UK STFC grants PP/C502406/1 and ST/F003072/1, grant GA ČR 205/08/0411, and the EU grant MRTN-CT-2006-035519. The Czech Academy of Sciences institutional research plan number is AV0Z10030501. We are very much indebted to all collaborators at the DFN stations for their work on this project. We also thank M. Cupák, M. Halík, J. Ullrich, A. Forte, M. Creasy, L. Beazley, T. Smith, C. Daw, T. Davies, T. Kennedy, G. Kennedy, W. Moore, P. Trepka, and the trustees of the Western Australian Museum for their help and support over the course of this project, and Australian Post for in-kind sponsorship. We also gratefully acknowledge helpful comments by the referees Dr. R. Hawkes and Dr. J. Vaubaillon.

Editorial Handling—Dr. A. J. Timothy Jull

REFERENCES

Beech M. 2002. The age of the Geminids: A constraint from the spin-up time-scale. *Monthly Notices of the Royal Astronomical Society* 336:559–563.

- Beech M., Illingworth A., and Murray I. S. 2003. Analysis of a "flickering" Geminid fireball. *Meteoritics & Planetary Science* 38:1045–1051.
- Benedix G. K., Bland P. A., Howard K. T., Spurný P., and Bevan A. W. R. 2010. The mineralogy and petrology of Bunburra Rockhole (abstract). 41st Lunar and Planetary Science Conference. p. 1438.
- Bland P. A. 2004. The Desert Fireball Network. *Astronomy & Geophysics* 45:20–23.
- Bland P. A., Spurný P., Towner M., Bevan A. W. R., Singleton A. T., Bottke W. F., Greenwood R. C., Chesley S. R., Shrbený L., Borovička J., Ceplecha Z., McClafferty T. P., Vaughan D., Benedix G. K., Deacon G., Howard K. T., Franchi I. A., and Hough R. M. 2009. An anomalous basaltic meteorite from the innermost Main Belt. Science 325:1525–1529.
- Bland P. A., Spurný P., Bevan A. W. R., Howard K. T., Towner M. C., Benedix G. K., Greenwood R. C., Shrbený L., Franchi I. A., Deacon G., Borovička J., Ceplecha Z., Vaughan D., and Hough R. M. 2012. The Australian Desert Fireball Network: A new era for planetary science. Thematic issue: Planetary Sciences. Australian Journal of Earth Science 59/2 (in press).
- Borovička J., Spurný P., Kalenda P., and Tagliaferri E. 2003. The Morávka meteorite fall: 1. Description of the events and determination of the fireball trajectory and orbit from video records. *Meteoritics & Planetary Science* 38:975–987.
- Brown P., Ceplecha Z., Hawkes R., Wetherill G., Beech M., and Mossman K. 1994. The orbit and atmospheric trajectory of the Peekskill meteorite from video records. *Nature* 367:624–626.
- Brown P. G., Hildebrand A. R., Zolensky M. E., Grady M., Clayton R. N., Mayeda T. K., Tagliaferri E., Spalding R. E., MacRae N. D., Hoffman E. L., Mittlefehldt D. W., Wacker J. F., Bird J. A., Campbell M. D., Carpenter R., Gingerich H., Glatiotis M., Greiner E., Mazur M. J., McCausland P. J. A., Plotkin H., and Rubak Mazur T. 2000. The fall, recovery, orbit, and composition of the Tagish Lake meteorite: A new type of carbonaceous chondrite. Science 290:320–325.
- Brown P., Pack D., Edwards W. N., ReVelle D., Yoo B. B., Spalding R. E., and Tagliaferri E. 2004. The orbit, atmospheric dynamics, and initial mass of the Park Forest meteorite. *Meteoritics & Planetary Science* 39:1781–1796.
- Brown P., McCausland P. J. A., Fries M., Silber E., Edwards W. N., Wong D. K., Weryk R. J., Fries M., and Krzeminski Z. 2011. The fall of the Grimsby meteorite—I. Fireball dynamics and orbit from radar, video, and infrasound records. *Meteoritics & Planetary Science* 46:339–363.
- Ceplecha Z. 1961. Multiple fall of Příbram meteorites photographed. 1. Double-station photographs of the fireball and their relations to the found meteorites. *Bulletin of the Astronomical Institute of Czechoslovakia* 12:21–47.
- Ceplecha Z. 1987. Geometric, dynamic, orbital, and photometric data on meteoroids from photographic fireball networks. Bulletin of the Astronomical Institute of Czechoslovakia 38:220–234.
- Ceplecha Z. 1996. Luminous efficiency based on photographic observations of the Lost City fireball and implications for the influx of interplanetary bodies onto Earth. *Astronomy & Astrophysics* 311:329–332.
- Ceplecha Z. and McCrosky R. E. 1976. Fireball end heights: A diagnostic for the structure of meteoric material. *Journal of Geophysical Research* 81:6257–6275.

- Ceplecha Z. and ReVelle D. O. 2005. Fragmentation model of meteoroid motion, mass loss, and radiation in the atmosphere. *Meteoritics & Planetary Science* 40:35–50.
- Ceplecha Z., Spurný P., Borovička J., and Keclícková J. 1993. Atmospheric fragmentation of meteoroids. *Astronomy & Astrophysics* 279:615–626.
- Chapman C. R. 2004. Space weathering and asteroid surfaces. Annual Review of Earth and Planetary Sciences 32:539–567.
- Gercek H. 2007. Poisson's ratio values for rocks. *International Journal of Rock Mechanics and Mining Sciences* 44:1–13.
- Halliday I., Blackwell A., and Griffin A. 1978. The Innisfree meteorite and the Canadian camera network. *Journal of the Royal Astronomical Society of Canada* 72:15–39.
- Hedin A. E. 1991. Extension of the MSIS thermospheric model into the middle and lower atmosphere. *Journal of Geophysical Research* 96:1159–1172.
- Hildebrand A. R., Milley E. P., Brown P. G., McCausland P. J.
 A., Edwards W., Beech M., Ling A., Sarty G., Paulson M.
 D., Maillet L. A., and Jones S. F. 2009. Characteristics of a Bright Fireball and Meteorite Fall at Buzzard Coulee, Saskatchewan, Canada, November 20, 2008 (abstract #2505). 40th Lunar and Planetary Science Conference. CD-ROM.
- Jenniskens P., Shaddad M. H., Numan D., Elsir S., Kudoda A. M., Zolensky M. E., Le L., Robinson G. A., Friedrich J. M., Rumble D., Steele A., Chesley S. R., Fitzsimmons A., Duddy S., Hsieh H. H., Ramsay G., Brown P. G., Edwards W. N., Tagliaferri E., Boslough M. B., Spalding R. E., Dantowitz R., Kozubal M., Pravec P., Borovička J., Charvát Z., Vaubaillon J., Kuiper J., Albers J., Bishop J. L., Mancinelli R. L., Sandford S. A., Milam S. N., Nuevo M., and Worden S. P. 2009. The impact and recovery of asteroid 2008 TC₃. Nature 458:485–488.
- McCrosky R., Posen A., Schwartz G., and Shao C. 1971. Lost City meteorites: Its recovery and a comparison with other fireballs. *Journal of Geophysical Research* 76:4090–4108.
- Paddack S. J. 1969. Rotational bursting of small celestial bodies: Effect of radiation pressure. *Journal of Geophysical Research* 74:4379–4381.
- Shrbený L. 2009. Meteor shower fireballs. Ph.D. thesis, Ondřejov Observatory, Ondřejov, Czech Republic.
- Shrbený L. and Spurný P. 2009. Precise data on Leonid fireballs from all-sky photographic records. Astronomy & Astrophysics 506:1445–1454.
- Skamarock W. C., Klemp J. B., Dudhia J., Gill D. O., Barker D. M., Duda M., Huang X.-Y., Wang W., and Powers J. G. 2008. A Description of the Advanced Research WRF Version 3. Boulder, Colorado. NCAR Technical note NCAR/TN-475+STR. 113 p.
- Spivak-Birndorf L. J., Bouvier A., Wadhwa M., Bland P. A., and Spurný P. 2010. Trace element geochemistry and chronology of Bunburra Rockhole basaltic achondrite (abstract #2274). 41st Lunar and Planetary Science Conference. CD-ROM. Meteoritics & Planetary Science 46.
- Spurný P. and Borovička J. 2002. The autonomous all-sky photographic camera for meteor observation. Proceedings of ACM 2002 Conference, ESA SP-500. pp. 257–259.
- Spurný P. and Ceplecha Z. 2008. Is electric charge separation the main process for kinetic energy transformation into the meteor phenomenon? *Astronomy & Astrophysics* 489:449–454.
- Spurný P., Oberst J., and Heinlein D. 2003. Photographic observations of Neuschwanstein, a second meteorite from the orbit of the Příbram chondrite. *Nature* 423:151–153.

- Spurný P., Borovička J., and Shrbený L. 2006. Automation of the Czech part of the European fireball network: Equipment, methods and first results. In *Proceedings of IAU Symposium 236*, edited by Valsecchi G. B., Vokrouhlický D., and Milani A. Cambridge, UK: Cambridge University Press. pp. 121–130.
- Spurný P., Bland P. A., Borovička J., Shrbený L., McClafferty T., Singelton A., Bevan A. W. R., Vaughan D., Towner M. C., and Deacon G. 2009. The Bunburra Rockhole meteorite fall in SW Australia: Determination of the fireball trajectory, luminosity and impact position from photographic records (abstract #1498). 40th Lunar and Planetary Science Conference. CD-ROM.
- Spurný P., Borovička J., Kac J., Kalenda P., Atanackov J., Kladnik G., Heinlein D., and Grau T. 2010. Analysis of instrumental observations of the Jesenice meteorite fall on April 9, 2009. Meteoritics & Planetary Science 45:1392–1407.
- Spurný P., Bland P. A., Shrbený L., Towner M. C., Borovička J., Bevan A. W. R., and Vaughan D. 2011. The Mason Gully meteorite fall in SW Australia: Fireball trajectory and orbit from photographic records (abstract #5101). 74th Meeting of the Meteoritical Society, August 8–12, 2011, London.
- Towner M. C., Duffy C. M., Bland P. A., Spurný P., and Abel R. L. 2010. The bulk properties of Bunburra

- Rockhole: Results of micro-CT scan analysis (abstract #1758). 41st Lunar and Planetary Science Conference. CD-ROM
- Towner M. C., Bland P. A., Spurný P., Benedix G. K., Dyl K., Greenwood R. C., Gibson J., Franchi I. A., Shrbený L., Bevan A. W. R., and Vaughan D. 2011. Mason Gully: The second meteorite recovered by the Desert Fireball Network. 74th Meeting of the Meteoritical Society, August 8–12, 2011, London. p. 5124.
- Trigo-Rodríguez J. M., Borovička J., Spurný P., Ortiz J. L., Docobo J. A., Castro-Tirado A. J., and Llorca J. 2006. The Villalbeto de la Pena meteorite fall: II. Determination of atmospheric trajectory and orbit. *Meteoritics & Planetary Science* 41:505–517.
- Welten K. C., Meier M. M. M., Caffee M. W., Laubenstein M., Nishizumi K., Wieler R., Bland P. A., and Spurný P. 2011. Cosmic-ray exposure age and pre-atmospheric size of the Bunburra Rockhole achondrite. *Meteoritics & Planetary Science* 46. This issue.
- Yano H., Kubota T., Miyamoto H., Okada T., Scheeres D., Takagi Y., Yoshida K., Abe M., Abe S., Barnouin-Jha O., Fujiwara A., Hasegawa S., Hashimoto T., Ishiguro M., Kato M., Kawaguchi J., Mukai T., Saito J., Sasaki S., and Yoshikawa M. 2006. Touchdown of the Hayabusa spacecraft at the Muses Sea on Itokawa. *Science* 312:1350–1353.